Title: Solar contributions to Earth's oceans

Authors: Luke Daly*[1,2,3,4], Martin R. Lee[1], Lydia J. Hallis[1], Hope A. Ishii[5], John P. Bradley[5], Phillip. A. Bland[2], David W. Saxey[6], Denis Fougerouse[2,6], William D. A. Rickard[6], Lucy V. Forman[2], Nicholas E. Timms[2], Fred Jourdan[2], Steven M. Reddy[2,6], Tobias Salge[7], Zakaria Quadir[8,9], Evangelos V. Christou[1], Morgan A. Cox[2], Jeffrey A. Aguiar[10,11], Khalid Hattar[12], Anthony Monterrosa[12], Lindsay P. Keller[13], Roy Christoffersen[14], Catherine A. Dukes[15], Mark J. Loeffler[16] and Michelle S. Thompson[17].

Affiliations:

[1]School of Geographical and Earth Sciences, University of Glasgow, Glasgow, G12 8QQ, UK.

[2]Space Science and Technology Centre, School of Earth and Planetary Sciences, Curtin University, GPO Box U1987, Perth, WA 6102, Australia.

[3]Australian Centre for Microscopy and Microanalysis, University of Sydney, Sydney 2006, NSW, Australia.

[4]Department of Materials, University of Oxford, Oxford, OX1 3PH, UK

[5]Hawaii Institute of Geophysics and Planetology, University of Hawai'i at Mānoa, Honolulu, HI, 96822.

[6]Geoscience Atom Probe Facility, Advanced Resource Characterisation Facility, John de Laeter Centre, Curtin University, GPO Box U1987, Perth, WA 6845, Australia.

[7]Imaging and Analysis Centre, Natural History Museum, Cromwell Road, London, SW7 5BD, UK.

[8]School of Civil and Mechanical Engineering, Faculty of Science & Engineering, Curtin University, GPO Box U1987, Perth, WA 6845, Australia.

[9]Microscopy & Microanalysis Facility, John de Laeter Centre, Curtin University, GPO Box U1987, Perth, WA 6845, Australia.

[10]Nuclear Materials Department, Idaho National Laboratory, Idaho Falls, ID USA.

[11]Advanced Technology Center, Lockheed Martin, Palo Alto, CA USA

[12]Sandia National Laboratories, PO Box 5800, Albuquerque, New Mexico, 87185, USA.

[13]Robert M Walker Laboratory for Space Science, Code KR, Astromaterials Research and Exploration Science, NASA Johnson Space Center, Houston, TX, 77058, USA

[14]Jacobs, NASA Johnson Space Center, Mail Code XI3, Houston, TX 77058, USA

[15]Laboratory for Astrophysics and Surface Physics, University of Virginia, Charlottesville, Virginia, 22904, USA

[16]Department of Astronomy and Planetary Science, Northern Arizona University, Flagstaff, Arizona, USA

[17]Department of Earth, Atmospheric and Planetary Sciences, Purdue University, West Lafayette, IN, 47907, USA.

*Correspondence to: luke.daly@glasgow.ac.uk

Summary:

The isotopic composition of water in Earth's oceans is challenging to recreate using a plausible mixture of known extraterrestrial sources such as asteroids - an additional isotopically light reservoir is required. The Sun's solar wind could provide an answer to balancing Earth's water budget. We used atom probe tomography to directly observe an average ~1 molecular percent enrichment in water and hydroxyls in the solar wind irradiated rim of an olivine grain from the S-type asteroid Itokawa. We also experimentally confirm that H irradiation of silicate mineral surfaces produces water molecules. These results suggest that the Itokawa regolith could contain ~20 litres per

m^3 of solar wind derived water and that such water reservoirs are likely ubiquitous on airless worlds throughout our galaxy. The production of this isotopically light water reservoir by solar wind implantation into fine grained silicates may have been a particularly important process in the early Solar System, potentially providing a means to recreate Earth's current, water-isotope ratios.

Main Text:

The origin of Earth's water and volatile budget is a topic of considerable debate in planetary science[1-10]. Most current dynamical models of Earth's formation assume that the majority of Earth's water and other volatiles was added later from an exogenous source[1-4]. That volatile source shared a common parent population with C-type asteroids, that is likely located in the Jupiter-Saturn region and beyond[11-14]. C-Type asteroids are thought to be the parent bodies of carbonaceous (C) chondrite meteorites as they exhibit similar reflectance spectra, in particular the CRs, CMs and CIs[15], which can contain up to 10 weight percent (wt. %) H_2O **(Table 1)**[9]. Although the D/H isotope ratios of C-chondrite meteorites are a closer fit to the Earth than to comets or other meteorite types, with CMs being a particularly close match **(Table 1)**[2,16], the Earth's mantle and Standard Mean Ocean Water (SMOW) are lighter in D/H[17] than the average of CI-, CR- and CM-chondrite groups [e.g., [1,16,18] **Table 1**]. Given the diversity of water rich C-chondrites in the meteorite record, it is unlikely that CM-like asteroids alone delivered all of Earth's water. Thus, as they are the most water-rich meteorites [9], the CIs, CRs and CMs are believed to represent the majority of Earth's chondritic water component. Although recent studies of nominally anhydrous minerals from enstatite chondrites[10] and Itokawa particles[19] suggests that these materials may be more water-rich than previously thought, they only contain sufficient water for the lowest estimate of Earth's water budget (**Table 1**). D/H ratios of the Earth's deep mantle are even lighter than SMOW **(Table 1)**[2]; recent analysis of volcanically exhumed material indicate that a component of

isotopically-light, solar-like D/H may be extant in the primitive mantle **(Table 1)**[6]. In addition, the bulk D/H ratio of the Earth may have increased from its initial value over the last 4.5 Ga potentially due to a preferential loss of the lighter hydrogen isotope to space[20]. However, increasing the D/H ratio via this mechanism is challenging to reconcile with extraterrestrial delivery of other isotope systems from C-type material e.g. Nitrogen[3]. Nevertheless, the volatile isotopic composition of the Earth is an enigma and it is likely that at least one other light isotope reservoir must have contributed to our planet's water budget - e.g., the Sun and/or the solar nebula.

The Sun could provide this additional reservoir, as it is isotopically light compared to SMOW and the bulk Earth **(Table 1)**[4]. It has been suggested that H adsorption onto mineral grain surfaces in the nebula[21] or dissolution of nebular H_2 into Earth's magma ocean[7,22] could have contributed a solar nebula D/H component. However, there are substantial challenges to this model[3] and the abundance of H deliverable by this mechanism is unconstrained and would only be a contributing factor while the gaseous nebula is present. A late veneer of the final 0.5 ± 0.25 % of Earth's mass[23-25], post core formation and after the gas disk had dissipated is likely to have contributed some of Earth's water from a predominantly chondritic source[11-14], but may still require a light D/H reservoir.

Intriguingly, volatile isotope ratios of hydrogen from the solar wind (e.g. $D/H = 2\times10^{-7}$ **(Table 1)**[26]), and the surfaces of materials that have been irradiated by solar wind, such as the samples recovered from NASA's GENESIS mission[27], have D/H isotope ratios consistent with the protosun and protosolar nebula[26,27]. The composition of the solar photosphere, and by extension the solar wind, is 96 % H and 4 % He, with the remaining ions comprised of all elements in their solar abundance ratios[28,29].

It has been demonstrated by observation and experimentation that solar wind irradiation of rocky materials results in a reaction between H ions and silicate minerals to produce OH and

98 water[5,30-34]. These molecules may become trapped in the 20-200 nm thick damage layer
99 induced by solar wind irradiation and other space weathering processes[30]. This phenomenon
100 could explain why the regoliths of airless worlds such as the Moon, which were once thought
101 to be anhydrous, contain several percent water[35-37]. Implantation of Solar H may also explain
102 why nominally anhydrous minerals in asteroids have water abundances of several hundred
103 parts per million[10,19] by weight. Clear evidence for these reactions also comes from the
104 detection of OH bonds and inferred water contents of up to 1 mol. % (where mol.% is
105 equivalent to the percentage of water molecules [sum total of H, OH and H_2O ions per 100
106 atoms of a material see **methods**), in the solar wind irradiated surfaces of interplanetary dust
107 particles (IDPs), as well as the production of water in minerals during laboratory space
108 weathering experiments[30,33]. These lines of evidence hint that a volatile reservoir isotopically
109 similar to the solar wind may have been present in the Solar System and contributed to
110 Earth's oceans. One potentially important source of such water, whose contribution has yet to
111 be quantitatively evaluated, is the regolith of silicate-rich asteroids and other fine-grained
112 extraterrestrial materials such as IDPs and the matrix of primitive chondrite meteorite. Such
113 materials comprise ~99% of the present day extraterrestrial mass flux[38]; they were produced
114 in high quantities through a variety of mechanisms including during impacts between
115 planetesimals, active outgassing or disruptive outbursts from comets and asteroids
116 bombardment by and collisions between IDPs, in the radiation-rich debris disk stage of a
117 protoplanetary disk[39-42], and so also during the late veneer stage of accretion of the terrestrial
118 planets.

119 Atom probe tomography (APT) is a quantitative analytical technique capable of measuring
120 the abundance of water and OH molecules within minerals in three dimensions at sub-
121 nanometre resolution[43]. We utilized APT to measure water abundances of space weathered
122 surfaces on both sides of a particle from the asteroid Itokawa (RA-QD02_0279) (**methods**

Fig. 1, S1, S2, S6-8) that was returned to Earth by JAXA's Hayabusa mission in 2011[44]. Our Itokawa APT data (**Fig. 2, S3, S5A-C**) are supported by results from analyses of the same particle by scanning electron microscopy (SEM) (**Fig. 1A-B, S1-2**), and transmission electron microscopy (TEM) (**Fig. 1C-E**). In addition, APT measurements of three experiments using San Carlos olivine (SCO) standard reference materials support this work. One pristine SCO sample was exposed to the laboratory atmosphere (PSCO), one was irradiated with He^+ (HeSCO) at 4 keV, and a third was irradiated with D^+ (DSCO) at 1 and 10 keV (**Fig 2D-J, S4, S5D and methods**). The energy used during the D^+ and He^+ irradiation experiments is consistent with that of the solar wind.

SEM images of the Itokawa grain show that its surface has an angular, pristine appearance and is free of micrometeorite impact craters (**Fig. 1A-B, S1-2**). TEM images of the particle indicate that it has a 40-50 nm thick solar wind irradiated rim that is crystalline and exhibits slight variations in density (**Fig. 1C-E**). The space weathered rim was sensitive to irradiation by the electron beam, resulting in a change in contrast, relative to the rest of the grain, which could be due to its volatile enrichment. No Fe nanoparticles were observed (**Fig. 1C-E**) in contrast to reports from other Itokawa grains[45] and APT analyses of Lunar ilmenite[46]. The properties of the solar wind irradiated surface and rim of this grain indicate that its space weathering features could be immature, maybe because it was exposed for a shorter period than other previously characterized space weathered Itokawa grains[45].

APT results from the Itokawa grain reveal that OH and water are enriched in the rims on both sides of the particle by 0.1-1.6 ± 0.05 molecular percent above background (Mol. %; where mol.% is equivalent to the percentage of water molecules [sum total of H, OH and H_2O ions per 100 atoms of a material see **methods**) (**Fig. 2A-C, S3, S5, and methods**). The depth of water implantation (40-180 nm) is consistent with Monte Carlo simulations of the penetration

147 depth of solar wind derived H^+ into silicate minerals at heliocentric distances of Itokawa[47],
148 and with our TEM observations (**Fig 1C-E**).

149 APT data revealed that there was no OH or H_2O enrichment in the near surface profile of the
150 PSCO grains, indicating that the signal in the Itokawa particle is not an artifact of sample
151 handling or laboratory analysis (**Fig S4V-X**). In contrast, the outermost 50 nm of the DSCO
152 sample is enriched with respect to D_2, DO and D_2O (**Fig. 2D-J, S4A-U, S5D**). While this rim
153 is similar in thickness to the space weathered profile of Itokawa, importantly no H was
154 generated by laboratory irradiation, and a substantially lower H and OH signal was observed
155 across the DSCO rim relative to the unirradiated bulk olivine portion of the DSCO sample
156 (**Fig 2D-J, S4A-U, S5D**). This DSCO result further confirms that heavy water can be
157 generated by D irradiation of silicate mineral surfaces, and therefore, H irradiation would
158 similarly generate water[5,30-34]. Additionally, the absence of H and OH in the rim of the D-
159 irradiated grain (**Fig. 2D-J, S4A-U, S5**) indicates that isotopic exchange of an irradiated grain
160 surface with the terrestrial atmosphere is minimal, at least over curatorial timescales. Thus,
161 APT results acquired from the SCO standard materials confirm that the Itokawa results are
162 not a consequence of sample preparation or terrestrial contamination and therefore must be
163 due to extraterrestrial processes, specifically solar wind implantation of volatiles (**methods,**
164 **Fig. 2D-J, S4, S5D**).

165 Despite the immature space weathering of the Itokawa grain (**Fig. 1, S1-2, [**[45]]), we observe
166 an implanted water enrichment (0.1-1.6 ± 0.05 mol. %) in its rims (**Fig. 2A-C, S3, S5A-C**).
167 These water abundances are similar to those detected in space weathered rims of a similar
168 thickness on the surfaces of silicate grains from IDPs[30]. Thus, comparable water abundances
169 have now been determined for two solar wind irradiated materials using two different
170 techniques, giving confidence in the enrichment level provided by both sets of measurements.
171 This measured water enrichment is interpreted as the 'saturated' value where solar wind

implantation is in equilibrium with volatile loss in the space environment through solar heating and prolonged (~8 Ma for Itokawa[48]) exposure to a vacuum[49]. Thus, using this water enrichment value (0.1-1.6 ± 0.05 mol. %) and assuming a space weathered rim thicknesses of 40-200 nm[30,47,50] for olivine and other silicate minerals, the overall water abundance imbibed into olivine grains of various sizes can be calculated (**Fig. 3, methods**). A space weathered spherical particle with a diameter of 100 μm, typical for most Itokawa regolith grains[44,45,47], would contain ~0.01 mol. % solar wind derived water (**Fig. 3**). Assuming that water enrichment by the solar wind is consistent between grains and minerals that comprise the regolith of Itokawa, every 1 m^3 of Itokawa regolith could contain up to ~20 litres of solar wind derived water. As such, solar wind irradiated silicate minerals may represent a substantial renewable source of water on airless worlds throughout the galaxy.

The abundance of water within a particular grain will depend its indigenous water constrained by its mineralogy, and source, and the abundance of solar wind derived water which is dependent on the particles grain size and shape. Most terrestrial olivine contains ~0.001-0.01 mol. % water (e.g. [51]). Itokawa regolith and ordinary chondrite silicates may be more water-rich throughout, where pyroxene grains from Itokawa, and pyroxene and olivine grains within ordinary chondrites and chondrule glasses within enstatite chondrites have measured water contents of 0.016-0.0998 mol. %[[10,19]]. Thus, assuming spherical particles >100 μm in size the solar wind contribution to their overall water budget would be < 50 %. Where ~100 μm in diameter, the solar wind derived water of a particle would represent at least half its total water budget, producing a nominally water-poor particle with an isotopic signal between the heavier chondritic values[1,16] and lighter solar values[4,27-29]. However, the solar wind derived component would constitute 0.1-1.6 mol. % water in particles <10 μm in diameter (**Fig. 3**), thus close to 100% of the water present in the grain.

196 Particle sizes of <10 μm are typical for the matrices of primitive chondritic meteorites[52,53],
197 IDPs[54], and cometary fragments from Wild 2 recovered by the Stardust mission[55]. At the
198 present-day, ~30,000 tons of small particles (submicrometre-mm with a peak at 200 μm)
199 thought to originate from comets, asteroids and IDPs fall to Earth each year[56-58] representing
200 99.9% of the annual delivery of extraterrestrial matter[38]; IDPs alone contribute ~1% of
201 Earth's current annual extraterrestrial input[58]. In addition, coarse >100 μm highly porous
202 aggregates such as IDPs[54] and fragments of chondritic matrix[52,53] that have a larger surface
203 area to volume ratio would also be substantially enriched in solar wind derived water and
204 may be comparable in solar wind derived water contents to <200 nm isolated grains.
205 Therefore, isolated grains in interplanetary space of similar size, irradiated by the solar wind,
206 could represent a significant source of isotopically light water in the Solar System.

207 Assuming that this particle size distribution is also representative of the debris disk stage of
208 Solar System formation, following the dissipation of the solar nebula where the disk would
209 have become transparent, then fine grained and/or porous particles in the IDP-chondritic
210 matrix size range, that are isotopically light and water-rich, may have been accreted alongside
211 planetesimal sized objects during the late veneer to contribute the final 0.5 ± 0.25 % of
212 Earth's mass. Since many of these particles are nano-composites of (organic) carbon and
213 silicate minerals[30,59], solar wind production of water at their surfaces may have been
214 accompanied by diversification of molecular chemistry. However, for fine grained materials
215 irradiated by the solar wind to have contributed significantly to the Earth's late veneer, dust
216 generation at this time period must have been greater than at the present day. Indeed,
217 observations of dusty debris disks in our Galaxy by WISE indicate that between 10^{-1} and 10^{-4}
218 Earth masses is present as micrometre sized dust [60]. Similar dust abundances present during
219 this stage of our own Solar System's formation. The dust would then have been accreted
220 alongside large chondritic asteroids. Very little dust, particularly fine grained materials, will

have remained in the protoplanetary disk once the nebular gas had dissipated[61]. However, substantial amounts of dust are observed in current debris-disks around nascent planetary systems[41] that likely formed by giant impacts e.g. [39-41], collisional cascades between ~100 km size bodies resulting in runaway collisions between progressively smaller asteroids and resulting in their complete disaggregation into micrometre sized dust[60], as well as active outgassing and disruptive outbursts from primitive asteroids and comets[42]. In addition, numerical modelling of the evolution of IDP size suggests that fine grained dust in the ~5 μm size range dominates the mass fraction of dust in the inner solar system at the expense of larger IDPs[42]. This would provide an abundance of fine grained particles implanted with a major component of solar wind derived water. Thus the abundance of fine grained particles like IDPs during this time period are expected to be orders of magnitude greater than the present day[56,62]. This newly formed dust would subsequently have been exposed to the solar wind to produce water before it was (re)accreted by the terrestrial planets and asteroids. An additional consideration is that during the debris disk stage of the early Solar System, particles would have experienced much more intense solar wind irradiation than at the present-day because, while the early Sun was much fainter during its formation, the solar wind flux was higher and more energetic[63,64]. This enhanced solar wind flux would be particularly significant during the energetic T-Tauri stage of our Sun[56]. Therefore, exposed small particles would have accumulated more water than at the present-day by virtue of elevated OH forming reactions with solar wind H ions and a thicker space weathered rim. Furthermore, the noble gas abundance and microstructural features of components within primitive chondrites that are consistent with paleo space weathering indicate that many primitive bodies formed from materials that experienced solar wind irradiation during the debris disk stage[65,66]. Many chondrites are breccias, while many asteroids are rubble piles[67] indicating that primitive asteroids may have experienced one, if not several, cycles of

accretion, disruption and re-accretion and thus would have incorporated solar wind derived water as they reaccreted fine grained materials that had been exposed to the radiation rich environment of the early Solar System. Thus, both fine grained dust, as well as the bodies onto which this dust accreted, contain significant solar wind generated water.

We have modeled the abundance and isotopic composition of water in four reservoirs: enstatite chondrites, water-rich chondrites (CM, CR and CI), ordinary chondrites and solar wind (**methods**). If only the average D/H ratio and water abundance of water-rich chondrite and solar wind contributions are considered, an addition of water from solar wind irradiated small particles of between 52-76% by mass is required alongside water-rich chondrites to produce Earth's D/H ratio (**Fig. 4**) during the late veneer. However, if only CM meteorites are considered, a 0% contribution by mass of solar wind derived water is required (**Fig. 4**). The water reservoir derived from solar wind irradiated fine grained particles and their calculated mass contribution to Earth during the late veneer, is substantially lower than the present-day (99% by mass) and past mass contribution of small particles relative to larger bodies over most of Earth's history[38] but may be consistent with the relative abundance of fine grained dust and larger planetesimals during the late veneer. In addition, our model predicts that contributions from enstatite chondrites and ordinary chondrites during late-stage accretion of the Earth would reduce the quantity of small solar wind irradiated particles required to account for terrestrial D/H ratios. However, the water-poor nature of these chondrites would still necessitate some contribution from fine grained particles that have been implanted with water by the solar wind for all but the lowest estimate of the water abundance of the Bulk Earth (**Table 1**). In this minimal terrestrial water scenario, no Solar wind derived water is required but a 96-94% contribution of enstatite or ordinary chondrite like material is required to provide the low D/H water contribution to Earth's water budget.

Our quantification of the magnitude of water enrichment in solar wind irradiated grains implies that accretion of a reservoir of volatile-rich small particles during the late veneer could reconcile the D/H isotopic composition of Earth's oceans. A contribution of water from solar wind irradiated small particles during the latter stages of Earth's accretion may be a key factor in reconciling the D/H ratio of Earth's final water budget. In addition, the continuous flux of small particles over Earth's history could help to reduce any isotopic fractionation of Earth's oceans by replacing any of the light isotopes of H that could be lost to space over time (e.g. [20]).

Main references

1 Alexander, C. M. O. D. The origin of inner Solar System water. *Phil Trans Royal Soc* **375**, 20150384 (2017).

2 Marty, B. The origins and concentrations of water, carbon, nitrogen and noble gases on Earth. *Earth & Planet Sci Lett* **313**, 56-66 (2012).

3 Meech, K. & Raymond, S. N. Origin of Earth's Water: Sources and Constraints. *Planet Astrobio*, 325 (2020).

4 Robert, F. The origin of water on Earth. *Sci* **293**, 1056-1058 (2001).

5 Greenwood, J. P. *et al.* Hydrogen isotope ratios in lunar rocks indicate delivery of cometary water to the Moon. *Nat Geo* **4**, 79-82 (2011).

6 Hallis, L. J. *et al.* Evidence for primordial water in Earth's deep mantle. *Sci* **350**, 795-797 (2015).

7 Ikoma, M. & Genda, H. Constraints on the mass of a habitable planet with water of nebular origin. *Astrophys J* **648**, 696 (2006).

8 Morbidelli, A. *et al.* Fossilized condensation lines in the Solar System protoplanetary disk. *Icarus* **267**, 368-376 (2016).

9 Morbidelli, A. *et al.* Source regions and timescales for the delivery of water to the Earth. *Met & Planet Sci* **35**, 1309-1320 (2000).

10 Piani, L. *et al.* Earth's water may have been inherited from material similar to enstatite chondrite meteorites. *Sci* **369**, 1110-1113 (2020).

11 O'Brien, D. P., Walsh, K. J., Morbidelli, A., Raymond, S. N. & Mandell, A. M. Water delivery and giant impacts in the 'Grand Tack'scenario. *Icarus* **239**, 74-84 (2014).

12 Raymond, S. N. & Izidoro, A. The empty primordial asteroid belt. *Sci Adv* **3**, e1701138 (2017).

13 Raymond, S. N., Quinn, T. & Lunine, J. I. High-resolution simulations of the final assembly of Earth-like planets I. Terrestrial accretion and dynamics. *Icarus* **183**, 265-282 (2006).

14 Walsh, K. J., Morbidelli, A., Raymond, S. N., O'Brien, D. P. & Mandell, A. M. A low mass for Mars from Jupiter's early gas-driven migration. *Nat* **475**, 206-209 (2011).

15 Bates, H., King, A., Donaldson Hanna, K., Bowles, N. & Russell, S. Linking mineralogy and spectroscopy of highly aqueously altered CM and CI carbonaceous chondrites in preparation for primitive asteroid sample return. *Met & Planet Sci* **55**, 77-101 (2020).

16 McCubbin, F. M. & Barnes, J. J. Origin and abundances of H2O in the terrestrial planets, Moon, and asteroids. *Earth & Planet Sci Lett* **526**, 115771 (2019).

17 Lécuyer, C., Gillet, P. & Robert, F. The hydrogen isotope composition of seawater and the global water cycle. *Chem Geol* **145**, 249-261 (1998).

18 Marty, B. *et al.* Origins of volatile elements (H, C, N, noble gases) on Earth and Mars in light of recent results from the ROSETTA cometary mission. *Earth & Planet Sci Lett* **441**, 91-102 (2016).

19 Jin, Z. & Bose, M. New clues to ancient water on Itokawa. *Sci Adv* **5**, eaav8106 (2019).

20 Genda, H. & Ikoma, M. Origin of the ocean on the Earth: early evolution of water D/H in a hydrogen-rich atmosphere. *Icarus* **194**, 42-52 (2008).

21 Asaduzzaman, A., Muralidharan, K. & Ganguly, J. Incorporation of water into olivine during nebular condensation: Insights from density functional theory and thermodynamics, and implications for phyllosilicate formation and terrestrial water inventory. *Met & Planet Sci* **50**, 578-589 (2015).

22 Sasaki, S. The primary solar-type atmosphere surrounding the accreting Earth: H 2 O-induced high surface temperature. *LPI*, 195-209 (1990).

23 Dauphas, N. & Marty, B. Inference on the nature and the mass of Earth's late veneer from noble metals and gases. *J Geophys Res: Planet* **107**, 12-11-12-17 (2002).

24 Day, J. M., Pearson, D. G. & Taylor, L. A. Highly siderophile element constraints on accretion and differentiation of the Earth-Moon system. *Sci* **315**, 217-219 (2007).

25 Walker, R. J. Highly siderophile elements in the Earth, Moon and Mars: update and implications for planetary accretion and differentiation. *Geochemistry* **69**, 101-125 (2009).

26 Huss, G., Nagashima, K., Burnett, D., Jurewicz, A. & Olinger, C. A new upper limit on the D/H ratio in the solar wind. *LPI*, 1709 (2012).

27 Geiss, J. & Gloeckler, G. in *Primordial Nuclei and their Galactic evolution* 239-250 (Springer, 1998).

28 Lodders, K. Solar system abundances and condensation temperatures of the elements. *Astrophys J* **591**, 1220 (2003).

29 Marty, B., Chaussidon, M., Wiens, R., Jurewicz, A. & Burnett, D. A 15N-poor isotopic composition for the solar system as shown by Genesis solar wind samples. *Sci* **332**, 1533-1536 (2011).

30 Bradley, J. P. *et al.* Detection of solar wind-produced water in irradiated rims on silicate minerals. *Proc Natl Acad Sci* **111**, 1732-1735 (2014).

31 Ichimura, A., Zent, A., Quinn, R., Sanchez, M. & Taylor, L. Hydroxyl (OH) production on airless planetary bodies: Evidence from H+/D+ ion-beam experiments. *Earth & Planet Sci Lett* **345**, 90-94 (2012).

32 Liu, Y. *et al.* Direct measurement of hydroxyl in the lunar regolith and the origin of lunar surface water. *Nat Geo* **5**, 779-782 (2012).

33 Lucey, P. *et al.* Understanding the lunar surface and space-Moon interactions. *Rev Min and geochem* **60**, 83-219 (2006).

34 Zhu, C. *et al.* Untangling the formation and liberation of water in the lunar regolith. *Proc Natl Acad Sci* **116**, 11165-11170 (2019).

35 Bandfield, J. L., Poston, M. J., Klima, R. L. & Edwards, C. S. Widespread distribution of OH/H2O on the lunar surface inferred from spectral data. *Nat Geo* **11**, 173-177 (2018).

36 Pieters, C. M. *et al.* Character and spatial distribution of OH/H2O on the surface of the Moon seen by M3 on Chandrayaan-1. *Sci* **326**, 568-572 (2009).

37 Sunshine, J. M. *et al.* Temporal and spatial variability of lunar hydration as observed by the Deep Impact spacecraft. *Sci* **326**, 565-568 (2009).

38 Pasek, M. & Lauretta, D. Extraterrestrial flux of potentially prebiotic C, N, and P to the early Earth. *Orig Life Evol Bios* **38**, 5-21 (2008).

39 Canup, R. M. Simulations of a late lunar-forming impact. *Icarus* **168**, 433-456 (2004).

365 40 Krot, A. N., Amelin, Y., Cassen, P. & Meibom, A. Young chondrules in CB
366 chondrites from a giant impact in the early Solar System. *Nat* **436**, 989-992 (2005).
367 41 MacGregor, M. A. *et al.* Constraints on planetesimal collision models in debris disks.
368 *Astrophys J* **823**, 79 (2016).
369 42 Poppe, A. R. An improved model for interplanetary dust fluxes in the outer Solar
370 System. *Icarus* **264**, 369-386 (2016).
371 43 Reddy, S. M. *et al.* Atom Probe Tomography: Development and Application to the
372 Geosciences. *GGR* **44**, 5-50 (2020).
373 44 Nakamura, T. *et al.* Itokawa dust particles: a direct link between S-type asteroids and
374 ordinary chondrites. *Sci* **333**, 1113-1116 (2011).
375 45 Noguchi, T. *et al.* Incipient space weathering observed on the surface of Itokawa dust
376 particles. *Sci* **333**, 1121-1125 (2011).
377 46 Greer, J. *et al.* Atom probe tomography of space□weathered lunar ilmenite grain
378 surfaces. *Met & Planet Sci* **55**, 426-440 (2020).
379 47 Noguchi, T. *et al.* Space weathered rims found on the surfaces of the Itokawa dust
380 particles. *Met & Planet Sci* **49**, 188-214 (2014).
381 48 Nagao, K. *et al.* Irradiation history of Itokawa regolith material deduced from noble
382 gases in the Hayabusa samples. *Sci* **333**, 1128-1131 (2011).
383 49 Crider, D. H. & Vondrak, R. Hydrogen migration to the lunar poles by solar wind
384 bombardment of the Moon. *Adv Space Res* **30**, 1869-1874 (2002).
385 50 Keller, L. P. & McKay, D. S. The nature and origin of rims on lunar soil grains.
386 *Geochim et Cosmochim Act* **61**, 2331-2341 (1997).
387 51 Demouchy, S., Jacobsen, S. D., Gaillard, F. & Stern, C. R. Rapid magma ascent
388 recorded by water diffusion profiles in mantle olivine. *Geol* **34**, 429-432 (2006).

52 Nuth III, J. A., Brearley, A. J. & Scott, E. R. in *Chondrites and the protoplanetary disk.* 675.

53 Bland, P. A. *et al.* Why aqueous alteration in asteroids was isochemical: High porosity≠ high permeability. *Earth & Planet Sci Lett* **287**, 559-568 (2009).

54 Rietmeijer, F. J. Size distributions in two porous chondritic micrometeorites. *Earth & Planet Sci Lett* **117**, 609-617 (1993).

55 Zolensky, M. E. *et al.* Mineralogy and petrology of comet 81P/Wild 2 nucleus samples. *Sci* **314**, 1735-1739 (2006).

56 Love, S. & Brownlee, D. A direct measurement of the terrestrial mass accretion rate of cosmic dust. *Sci* **262**, 550-553 (1993).

57 Anders, E. Pre-biotic organic matter from comets and asteroids. *Nat* **342**, 255-257 (1989).

58 Flynn, G., Keller, L., Jacobsen, C. & Wirick, S. An assessment of the amount and types of organic matter contributed to the Earth by interplanetary dust. *Adv Space Res* **33**, 57-66 (2004).

59 Ishii, H. A. *et al.* Multiple generations of grain aggregation in different environments preceded solar system body formation. *Proc Natl Acad Sci* **115**, 6608-6613 (2018).

60 Vican, L. & Schneider, A. The evolution of dusty Debris disks around solar type stars. *Astrophys J* **780**, 154 (2013).

61 Wyatt, M. The insignificance of PR drag in detectable extrasolar planetesimal belts. *Astron & Astrophys* **433**, 1007-1012 (2005).

62 Nesvorný, D. *et al.* Cometary origin of the zodiacal cloud and carbonaceous micrometeorites. Implications for hot debris disks. *Astrophys J* **713**, 816 (2010).

63 Ayres, T. R. Evolution of the solar ionizing flux. *J Geophys Res: Planet* **102**, 1641-1651 (1997).

64 Kass, D. & Yung, Y. L. Loss of atmosphere from Mars due to solar wind-induced sputtering. *Sci* **268**, 697-699 (1995).

65 Suess, H., Wänke, H. & Wlotzka, F. On the origin of gas-rich meteorites. *Geochim et Cosmochim Act* **28**, 595-607 (1964).

66 Krietsch, D. *et al.* Noble gases in CM carbonaceous chondrites: Effect of parent body aqueous and thermal alteration and cosmic ray exposure ages. *Geochim et Cosmochim Act* (2021).

67 Walsh, K. J. Rubble pile asteroids. *Annual Review of Astronomy and Astrophysics* **56**, 593-624 (2018).

Acknowledgments: The authors would like to thank Dr. Martin Suttle for the preparation and loan of the mounting rod, and Dr. Ryan Ickert for providing access to the clean lab facility at the Scottish Universities Environmental Research Centre to mount the Itokawa particles and Ms Rasika Mahajan for providing a suitably fine-grained basaltic fragments to practice on. L.D. would also like to thank NASA JSC and the Lunar and Planetary Institute for the training received at the 4th training in the extraterrestrial sample handling course. The authors would also like to thank the three anonymous reviewers and editor Dr. Marios Karouzos for their thoughtful, insightful and constructive comments that vastly improved this manuscript. **Funding:** This work was funded by the UK STFC consortium grant, and UAE seed grant awarded to MRL, as well as a SAGES small grant awarded to LD. HI and JB were partially supported by the NASA LARS Program (80NSSC18K0936). This work was partially supported in part through the INL Laboratory Directed Research & Development (LDRD) Program under DOE Idaho Operations Office Contract DE-AC07-05ID145142 that supported JAA. This work was conducted within the Geoscience Atom Probe Facility at Curtin University, which is part of the Advanced Resource Characterization Facility (ARCF).

439 The Advanced Resource Characterization Facility is being developed under the auspices of
440 the National Resource Sciences Precinct – a collaboration between CSIRO, Curtin University
441 and The University of Western Australia – and is supported by the Science and Industry
442 Endowment Fund (SIEF RI13-01). The authors acknowledge the use of Curtin University's
443 Microscopy and Microanalysis Facility, whose instrumentation has been partially funded by
444 the University, State and Commonwealth Governments. This work was performed, in part, at
445 the Center for Integrated Nanotechnologies, an Office of Science User Facility operated for
446 the U.S. Department of Energy (DOE) Office of Science. Sandia National Laboratories is a
447 multi-mission laboratory managed and operated by National Technology and Engineering
448 Solutions of Sandia, LLC, a wholly owned subsidiary of Honeywell International, Inc., for
449 the U.S. DOE's National Nuclear Security Administration under contract DE-NA-0003525.
450 The views expressed in the article do not necessarily represent the views of the U.S. DOE or
451 the United States Government.

452 **Author contributions:** LD conceived the project with input from MRL. Itokawa sample
453 handling and mounting was conducted by MAC and LD. Itokawa SEM analysis was
454 conducted by TS MAC and LD. HI and JB prepared the polished SC olivine on Ta for D_2^+
455 irradiation. JA arranged and advised instrumentation for D_2^+ irradiation. KH and AM
456 performed D_2^+ irradiations. LPK, RC, and MST prepared the polished SC olivine for He^+
457 irradiation and CAD and MJL conducted the irradiation. LD and SMR prepared the polished
458 SC olivine and conducted the laboratory exposure. Cr coating was undertaken by WDAR, DF
459 and LD FIB preparations for TEM and APT was undertaken by LD, DF, WDAR. TEM work
460 was conducted by ZA, LD and WDAR. APT analysis was undertaken by DS, DF and LD.
461 Interpretation of the results was conducted by LD, PAB, LVF, MRL, LJH, NET, FJ, DWS
462 and DF. LD, HI, and WDAR, wrote the methods. LD wrote the manuscript with input from
463 all co-authors.

Main Figure legends

Fig. 1. SEM and TEM analyses of the space weathered (SW) surface of Itokawa particle RA_QD02_0279. (A) and (B) Secondary electron images of the front and rear surfaces, respectively, of the particle. Boxes indicate extraction locations of TEM (red) and APT (orange) samples. (C) TEM EDS Fe Kα X-ray map of the grain surface. Fe-nanoparticles are absent, and subtle variations in Fe X-ray signal are due to contrasting density through the rim, not compositional variations. The protective Cr coat, space weathered rim (SW) and unweathered olivine (Ol) are labelled. (D) Bright-field TEM image of the outermost part of the olivine grain and Cr coat. The 50 nm thick SW rim is readily apparent beneath the grain surface and is delineated by two dashed white lines. The patchy contrast of the rim indicates variations in the intensity of electron scattering and density, but not in composition. (E) High Angle Annular Dark Field (HAADF) TEM image of the protective Cr coat, SW rim and unweathered olivine (Ol). Lattice fringes with a 0.35 nm spacing, probably {120} planes (yellow), extend through the SW rim indicating that it is at least in part, crystalline.

Fig. 2. Representative APT data from Itokawa particle RA_QD02_0279 (A-C) and DSCO (D-J). All data sets extend from the Cr protective layer (grey spheres) through the space weathered surface and into unweathered olivine. (A) APT measurement of the 3D distribution of Cr (grey spheres) and OH ions (teal spheres). (B) APT measurement of the 3D distribution of Cr and H_2O ions (blue spheres). (C) Concentration of ions in atomic percent (at. %; number of atoms per 100 atoms) with depth across the Cr capping layer (Cr, grey shaded region) space weathered rim (SW, blue shaded region) and the non-space weathered olivine (Ol, green shaded region) deeper into the mineral revealing variations in the

488 abundances of Cr (grey line), H (yellow line), OH (green line) and H_2O (blue line) ions. Line
489 widths have been adjusted to represent the 1 sigma uncertainty and depth profiles are absolute
490 abundances not relative concentrations (**Data S1**). The boundary between the Cr and SW
491 layer is marked by a vertical dashed red line and the boundary between the SW and Ol layer
492 is marked by a vertical black dashed line. (D-I) APT measurements of the 3D distribution of
493 ions through a typical DSCO sample. In all images, the Cr ions are show together with one
494 other ion. (D) D ions (purple spheres). (E) D_2 ions (orange spheres). (F) H ions (yellow
495 spheres). (G) DO ions (green spheres). (H) D_2O ions (turquoise spheres). (I) OH ions (teal
496 spheres). (J) Concentration of ions in at. % measured by APT of a DCSO sample with depth
497 across the Cr capping layer (Cr, grey shaded region) Deuterium irradiated rim (DI, blue
498 shaded region) and the non-Deuterium irradiated olivine (Ol, green shaded region) deeper
499 into the mineral revealing the variation in the abundance of Cr (grey line), D (purple line), D_2
500 (orange line), DO (red line), D_2O (blue line), H (yellow line), and OH (green line) ions. Line
501 widths have been adjusted to represent the 1 sigma uncertainty and depth profiles are absolute
502 abundances not relative concentrations (**Data S1**). The boundary between the Cr and DI layer
503 is marked by a vertical dashed red line and the boundary between the DI and Ol layer is
504 marked by a vertical black dashed line.

505

506 **Fig. 3. Graph of particle diameter vs abundance of water in atomic percent (mol. %)**
507 **generated by solar wind irradiation.** A variety of extraterrestrial materials are shown, each
508 of which has a space weathered rim of different thickness: (1) Lunar soil (200 nm, dark blue
509 line); (2) IDPs and maturely space weathered Itokawa particles (100 nm, light blue line); (3)
510 the sub-mature Itokawa grain in this study (50 nm, green line); (4) a very thin space
511 weathered surface (10 nm, red line). Representative grain sizes and water abundances for
512 different extraterrestrial materials are labelled on the graph. We assume a spherical particle in

513 all cases, and as such they represent the minimum solar wind derived water contents for
514 particles of these diameters. Fractal grains will have a larger surface area and therefore a
515 greater solar wind irradiation derived water component. Particles <1 μm can entrain and store
516 several mol. % of water derived from solar wind irradiation.

517

518 **Fig. 4. Diagram of the D/H ratio that results from mixing solar wind irradiated fine**
519 **grained particles and chondritic water reservoirs.** The D/H ratio plot is generated by
520 mixing water reservoirs of carbonaceous chondrite (CR[green volume], CI [blue volume],
521 CM [orange volume], Cav [red volume, the average of CR,CI and CMs D/H =
522 0.000173[[1,16]]; water abundance = 2-16 molecular % per atom[[9]]), ordinary chondrite (
523 purple volume, OC)[19] and enstatite chondrite (brown volume, EC)[10] material, and small
524 (<100 μm) space weathered particles (D/H = 0.0000002[[26]]; water abundance = 0.1-1.6
525 molecular % per atom that can reproduce the SMOW and Bulk Silicate Earth (BSE) D/H
526 ratio[1,17] (horizontal black dashed lines **Data S3)**. The upper and lower bounds of each colored
527 field represent the upper and lower limits of the water content within the chondrites and solar
528 wind irradiated particles. The relative mass contributions that span BSE and SMOW D/H
529 ratios indicates the range of potential mixtures of theses extraterrestrial water reservoirs that
530 could generate the present-day D/H of Earth's oceans. We also plot D/H ratio produced by
531 the mixture of EC vs Cav material (pink line).

532

533 **Table 1: Summary table of the D/H ratio and water abundance in wt. % and mol. %* of**
534 **extraterrestrial and terrestrial materials.** Data from this study and [1,2,4,6,10,16,18,19,26,68-72].
535 Uncertainties are one sigma.

536

Methods

Sample preparation

Itokawa

Itokawa particle RA-QD02-0279 was mounted on the end of a glass rod with resin (**Fig. 1A-B**) in the Pb clean lab facility at the Scottish Universities Environmental Research Centre (SUERC). The mounting rod is a typical micro-computed tomography sample mount and was prepared at the Natural History Museum, London, by drilling a hole in the top of a pin and placing a 100 μm diameter glass rod inside the hole and sealing it with wax. A drop of resin was used to affix the Itokawa grain to the apex of the glass rod to provide access to the majority of the sample's surface. The sample has been stored in contact with the terrestrial atmosphere since it was received from the Japanese Aerospace Exploration Agency (JAXA) Hayabusa Curation facility on the 30th June 2017.

San Carlos olivine (SCO)

To corroborate the Itokawa atom probe tomography (APT) results a set of pristine and irradiated San Carlos olivine (SCO) reference materials were produced.

Pristine SCO

One fragment of SCO (PSCO) was mounted in resin and polished flat with a water based polishing suspension. PSCO was dried and exposed to the terrestrial atmosphere in the laboratory for several months.

Deuterium-Irradiated San Carlos Olivine (DSCO)

Preparation for Irradiation

561 Saw-cut slices of a single crystal of SCO, 2-3 mm in thickness, were hand polished to 1 μm
562 and diced into pieces approximately 2-3 mm on a side. These SCO pieces were separated into
563 two sets of six sub-samples, set A and set B. Each set was mounted polished-side-up onto a
564 25 x 25 x 1 mm thick Ta foil (99.9% purity, Goodfellow) using pieces of adhesive carbon
565 conductive tabs (Pelco, Ted Pella) cut to match the size of each sample. The high atomic
566 number metal foil and limited extent of the carbon adhesive were chosen in order to minimize
567 potential sputter cross-contamination of the polished olivine surfaces during irradiation.
568
569 *Deuterium irradiation of SCO samples (DSCO)*
570 Deuterium irradiation of all DSCO samples was performed using a 10 kV Colutron G-1 ion
571 accelerator at the Sandia National Laboratories Ion Beam Laboratory. Two irradiation
572 experiments were performed at nominally room temperature with D_2^+ ions with energies of
573 10 keV (for set A) and 2 keV (for set B). The D_2^+ ions disassociate upon contact with the
574 surface and are implanted as a charged and uncharged D isotope, each with half the energy (5
575 keV and 1 keV, respectively).
576
577 The samples for each irradiation experiment were mounted at once in the *ex situ* irradiation
578 chamber, which was pumped down to a vacuum of ~10^{-7} torr. No heating or cooling elements
579 were utilized during the experiment, and beam heating was expected to be minimal. The
580 deuterium beam was continuous and focused to about 5 mm, and each sample was irradiated
581 to a fluence of approximately 10^{19} ions/cm^2. The fluence was determined by measuring the
582 current impinging on the stage during the experiment.
583
584 *DSCO Sample Transport*

585 Adsorbed and absorbed water is not a major concern because the isotopic signature of
586 deuterium is distinguishable from that of hydrogen. Nevertheless, irradiated surfaces are
587 generally hygroscopic, and we sought to minimize uptake of ambient water vapor during
588 transporting of the samples between University of Hawai‘i at Mānoa, Sandia National
589 Laboratories, University of Glasgow and Curtin University. DSCO samples were stored
590 together with a desiccant canister (DriCan, Ted Pella) in a sealed container (Spi-Dry sample
591 preserver, SPI Supplies) back-filled with dry Ar gas prior to and following deuterium
592 irradiation. Pairs of sub-samples from sets A and B were placed in membrane boxes with a
593 hole in one side and then vacuum packed with desiccant beads for expedited shipping for
594 APT experiments.
595
596 *Helium-Irradiated San Carlos Olivine (HeSCO)*
597 Single-crystal olivine was irradiated with 4 keV He^+ under ultra-high vacuum in a specialized
598 surface science instrument (PHI 560; P= 9 x 10^{-10} Torr) at the University of Virginia,
599 described in previous publications (e.g. [73,74]). The olivine mineral was cleaved in air, prior to
600 insertion into vacuum and mounted on a copper plate. X-ray photoelectron (XPS) spectra
601 were taken prior and post irradiation at regular fluence intervals, confirming chemical
602 reduction ($Fe^{3+} \rightarrow Fe^{2+} \rightarrow Fe^0$) of iron with simultaneous preferential removal of oxygen and
603 (atmospheric) carbon atoms. Helium ions were generated in an electron-bombardment source
604 at 4 kV and rastered over 6 x 6 mm^2 for uniform irradiation, providing an average flux of 4.9
605 x 10^{13} ions cm^{-2} s^{-1} to a final fluence of 9.2 x 10^{17} He^+ cm^{-2}. A low-energy electron flood gun
606 was used during irradiation to neutralize surface charge. Samples were then removed from
607 vacuum and stored at atmosphere, before subsequent transport to NASA Johnson Space
608 Center for analytical electron microscopy and focused ion beam (FIB) sectioning followed by
609 transport to Curtin University.

610

611 **High vacuum low kV scanning electron imaging**

612 Low accelerating voltage scanning electron microscopy (SEM) surface imaging including
613 secondary electron images of Itokawa particle RA-QD02-0279 was undertaken to identify
614 mineral phases and space weathering features such as micrometeorite impact craters (**Fig.**
615 **1A-B, S1-2**) to target for subsequent analysis. A low accelerating voltage (5-15 keV) was
616 used to minimize the possibility of mobilizing volatile phases and devolatilizing the space
617 weathered surfaces of these particles. SEM characterization of particle RA-QD02-0279 was
618 undertaken on the Tescan Mira3, variable pressure field emission gun (VP-FEG)-SEM at the
619 John De Laeter Centre, Curtin University.

620

621 **Focused ion beam (FIB)-SEM sample preparation for transmission electron microscopy**
622 **(TEM) and APT**

623 All samples were coated with 200 nm of Cr using a Cressington 208HR sputter coater at the
624 John de Laeter Centre, Curtin University. Coating thickness was determined using a crystal
625 thickness monitor and the 200 nm Cr coating was achieved by depositing eight 25 nm layers
626 with a 2-minute pause between layers to minimize sample heating. The Cr coating was
627 applied in order to protect the samples during focused ion beam (FIB)-SEM sample
628 preparation for APT and transmission electron microscopy (TEM), as well as to function as a
629 fiducial marker for the location of the grain surface in FIB-SEM preparation and within the
630 APT datasets. Cr was chosen due to the low concentration of Cr in olivine and because it has
631 a similar ionization potential to silicate phases. Therefore, during APT analysis the voltage
632 and laser energy required to achieve stable field evaporation between these two materials will
633 be similar and will minimize the risk of analysis artefacts and failure.

Several specimens of each sample (Itokawa RA-QD02-0279: front [5, **Fig. 1A and S1**] and back [5; **Fig. 1B, S2**]; PSCO [5]; and DSCO [5], were prepared for APT using the Tescan Lyra3 dual beam FIB-SEM at the John De Laeter Centre, Curtin University following the typical lift out method described in detail in Thompson et al., [75]. Additionally, one 5×10×0.1 µm TEM sample was extracted from Itokawa particle RA-QD02-0279 using the Tescan Lyra3 dual beam FIB-SEM at the John De Laeter Centre, Curtin University. This FIB-SEM uses a mono-isotopic liquid metal ion source of $^{69}Ga^{+}$ as a high precision milling beam. In brief, APT specimens were prepared from the region of interest in each sample by depositing a protective layer (2.5×10 µm) of Pt, firstly by electron beam deposition (200 nm thick) and then by ion beam deposition (1 µm). This layer was then undercut using the FIB to produce a wedge 15 µm in length. One end was cut free and attached to a micromanipulator with a Pt weld. The specimen was then cut free from the main mass of the sample and extracted. Prism shaped segments with 2.5 µm top edges of the wedge were placed, point down, so as the space grain surface of the sample was facing up, onto a pre-grown silica post on a microtip coupon with a Pt deposition and cut free. This process was repeated until all the wedge had been placed on posts. The samples were then shaped using a progressively smaller annular milling pattern and lower beam current in order to produce a fine <100 nm tip diameter needle specimen. Care was taken to ensure all the Pt was milled away but a small amount (~50 – 100 nm) of Cr remained at the tip of the needle to ensure the preservation of original surface (**Fig. S1C-H, 2D-H**). A final milling process at 2 kV accelerating voltage was performed to remove the top ~20 nm of damaged material produced by the high energy Ga^{+} ion implantation.

TEM methods

The electron transparent lamella was used for transmission electron microscopy (TEM) analysis on a FEI Talos FS200X G2 TEM/scanning TEM (STEM) microscope operated at 200 kV and equipped with a Super-X energy dispersive X-ray spectrometer (EDS) system located in the John de Laeter Centre in Curtin University. Bright Field (BF) imaging was used for high magnification imaging. STEM images and EDS data were captured with a beam current of 0.6 nA. STEM imaging included BF, Dark Field (DF) and High Angle Angular Dark Field (HAADF) imaging modes. EDS data was collected using FEI Velox software version 2.4.

Atom probe tomography

All APT specimens were analysed on the Cameca Local Electrode Atom Probe (LEAP) 4000X HR Geoscience atom probe, housed at the John de Laeter Centre, Curtin University. The analytical conditions for each run can be found in **Fig. S8**. All analyses were performed in laser assisted mode using an ultraviolet laser (λ = 355 nm). Four samples from Itokawa particle RA-QD02-0279 (two front **Fig. S1E, G**, [Itokawa1 and Itokawa2] and two back **Fig. S2F, H** [Itokawa4 and Itokawa3]), one sample from PSCO and three samples from DSCO ran successfully in the APT (**Fig. 2, S3-4)**. These APT samples all initially began field evaporation in the Cr capping layer before passing through any rim feature and into the main material.

The bulk composition of each APT specimen was calculated by measuring the full width half maximum of peaks in the mass to charge spectrum (**Fig. S5**). The same range file was used for all APT samples with additional peaks attributed to the DSCO datasets for D, D_2, DO and D_2O. The counting statistical uncertainty for each measured ion peak within the APT datasets was established through the formula below from [76].

$$s = \sqrt{A + B}$$

683 Where s is the counting statistical uncertainty, A is the total counts beneath a ranged peak
684 including background and B is the average background counts over the same range. These
685 uncertainties were propagated throughout. In all cases the uncertainties calculated in this way
686 were low (<5 %) and had negligible impact on the implications of the study.
687 Additional sources of uncertainty in APT data that should be considered are derived from
688 detector dead times[77-79]. However, this is only a significant consideration when reporting
689 isotope abundances for light elements. As such it is not accounted for in the present study
690 which only reports major element and molecular abundances.
691 Features present in the sample surface such as chemical profiles were identified in APT
692 datasets by producing a depth profile using a cylindrical region of interest across the Cr cap
693 and the sample material summing the elemental molecular concentrations over 2 nm bin sizes
694 (**Data S1**). Additionally, density fluctuations in the surface of the material were identified
695 through generating isosurfaces related to the density of ions collected for each element.
696
697 <u>The bulk olivine</u>
698 In all Itokawa APT olivine samples, $^{1}H^{+}$ (~1 u/Q; u = unified atomic mass unit, 1 u is 1/12 of
699 the mass of ^{12}C and Q = the charge in Coulombs) steadily increases with depth within the
700 olivine (**Fig. 2A-C, S3**). This signal is generated by adsorption of residual H on the specimen
701 surface in the UHV chamber and should be considered as noise. This background H level is
702 dependent on a number of factors such as tip shape, the material that is field evaporating, the
703 field around the needle, the temperature and humidity and so can vary between analysis of the
704 same material[80]. The increase of $^{1}H^{+}$ with analysis depth (**Fig. 2, S3, S4**) is commonly
705 observed in APT datasets and is due to the increasing field around the sample generating
706 more H evaporation from the chamber as the radius of the specimen and the voltage increase
707 during analysis. In addition to $^{1}H^{+}$ we also observe other water group ions within the mass

spectrum such as $^{16}O^{1}H^{+}$ (17 u/Q) $^{16}O^{1}H_2^{+}$ (18 u/Q) $^{16}O^{1}H_3^{+}$ (19 u/Q) (**Fig. 2, S3-5**) and these peaks are used for the quantification of the total water content within the APT datasets. This steady enrichment of H is also observed for $^{16}O^{1}H^{+}$ (17 u/Q) (**Fig. 2, S3-5**) as some of the H within the UHV forms a complex molecular ion with O to produce OH, this trend is also typical for O bearing APT datasets. The mass peak at 17 u/Q is predominantly comprised of OH. ^{17}O is only 0.04% of the total oxygen[28] and so the contribution of ^{17}O will be below background levels as such we assume the entire 17 u/Q peak is comprised of OH ions. All other ranged ions within the samples remain at a constant level throughout the olivine component of the datasets. As will be discussed later there is a distinct drop in the abundance of H and hydroxyl ions in all Itokawa APT data sets between 40-180 nm (**Fig. S3)** from the olivine grain surface. This drop cannot be generated by a change in the field and is a real property of the H content of the mineral.

The total abundance of H and OH is not constant between APT analysis of the same material as such each sample must be corrected separately. The mass peak at 18 u/Q is a result of the combination of ^{18}O and H_2O ions, ^{18}O is 0.2% of the total oxygen[28] so will have some contribution to the 18 u/Q peak in addition some of the H_2O ions will be derived from the combination of ^{16}O with H_2 from the UHV chamber. The mass peak at 18 u/Q was deconvolved to extract the $^{1}H_2{}^{16}O^{+}$ contribution from the $^{18}O^{+}$ signal assuming a solar $^{16}O/^{18}O$ ratio[28](*9*) to determine the total contribution form H_2O ions to the 18 u/Q peak. To calculate the average and maximum total content over the Itokawa samples and the deuterated water content of the DSCO samples, all relevant H (H, H_2, H_3, H_4, OH, H_2O H_3O) species or D (D, D_2, OD, D_2O) species respectively were ranged using the full width of the peak. To determine the total water component of the bulk olivine, atomic % (at. %; number of atoms per 100 atoms) totals for each species were calculated by determining the proportion of atoms relative to the total number of atoms under ranged peaks in each dataset extracted

733 from a volume of interest within the bulk olivine material away from any irradiated surface or
734 Cr interface (typically the volume defined by the final 20 nm of the analysis). The sum of the
735 measured at. % of all relevant H species were added together to produce molecular % (mol.
736 %) totals for water, where mol. % is the number of molecules of water per 100 atoms. From
737 these calculations we can determine that Itokawa olivine APT datasets comprise ~0.5 ± 0.05
738 mol. % water, DSCO comprise ~0.5 ± 0.05 mol. % water, and PSCO comprise ~0.6 ± 0.05
739 mol. % water. The water abundance in the bulk olivine of Itokawa DSCO and PSCO is
740 substantially higher than the 100-300 parts per million by weight water content measured
741 from bulk olivine in Itokawa grains, LL chondrites and terrestrial olivine[45,51]. This indicates
742 that the majority of the calculated bulk olivine water content in these APT data sets are
743 derived from surface reactions with H_2 in the UHV. This represents a normal UHV
744 contribution of water to the total abundance in each APT sample and allows us to detect
745 deviations from this normal level within the rest of the dataset. To do this, a cylindrical
746 region of interest was generated through each APT data to produce an at. % concentration
747 depth profile (**Fig. 2, S3, S4, S6, Data S1**) This is an absolute concentration and not a relative
748 abundance as such variations in minor species are not a result of heterogeneity in major
749 species. The data was averaged over 2 nm thick segments. The average background H (mol.
750 %) sum of all H or D species was generated from a summed average of all relevant species
751 from the basal 10 nm of the sample well within the olivine and away from the irradiated
752 surfaces as a proxy for the typical APT background. It should be noted that even D species
753 have a nominal background from isobaric interferences with H species. This background
754 water level was subtracted from the water content of each 2 nm segment to generate a real
755 water signal. The average water content was then calculated from the irradiated rims.
756
757 Irradiated surfaces

There is no variation within the PSCO for any ion species approaching the olivine grain surface (**Fig. S4V-X**). In particular, the H remains constant within the PSCO olivine grain surface (**Fig. S4V-X**). Within the DSCO and Itokawa APT data sets, the H abundance diminishes slightly within the space weathered or artificially irradiated rim (**Fig. 2, S3, S4A-N**). This depletion of H ions is more pronounced within the DSCO. In addition, OH (17 u/Q) is also depleted within the DSCO surface (**Fig. 2D-J, S4A-N**). This enhanced depletion of H in the DSCO is likely caused by the presence of D and corresponding absence of H. Within the DSCO, there is a pronounced 2-3 mol % enrichment in D (2 u/Q), D_2 (4 u/Q) DO (18 u/Q) and D_2O (20 u/Q) in the outermost 40 nm of the grain (**Fig. S4A-N, S5D**). In the Itokawa sample, APT data enrichments in H_2O and OH are observed in the upper 40-60 nm of the sample (**Fig. S3, S5A-C**). To calculate the total average water content in the space weathered rim, the sum of the 17, 18 and 19 u/Q peaks representing $^{17}O^{+}+{}^{1}H^{16}O^{+}$, $^{18}O^{+}+{}^{1}H_2{}^{16}O^{+}+{}^{1}H^{17}O^{+}$ and $^{1}H_3{}^{16}O^{+}+{}^{1}H_2{}^{17}O^{+}+{}^{1}H^{18}O^{+}$ respectively was averaged over the depth of the enrichment, while the total maximum water enrichment was measured from the maximum value detected within the rim. The average water content calculated previously from the bulk olivine was then subtracted from this value to give the total average water, and total maximum water derived from solar wind irradiation. Revealing a maximum of 1.6 mol. % (**Fig. S1E**), 1.4 mol. % (**Fig. S1G**), 0.24 mol. % (**Fig. S2F**), 0.7 mol. % (**Fig. S2H**) total enrichment in water species and an average of 0.8 mol. % (**Fig. S1E**), 0.7 mol. % (**Fig. S1G**), 0.16 mol. % (**Fig. S2F**), 0.47 mol. % (**Fig. S2H**) total enrichment in water species in the upper 50 nm (**Fig. S1E**), 60 nm (**Fig. S1G**), 180 nm (**Fig. S2F**), and 30 nm (**Fig. S2H**) of the grain (**Fig. S3**).

Sputter coated Cr layer

782 The H peak decreases substantially in the Cr cap within the DSCO and Itokawa samples but
783 increases within the PSCO APT dataset (**Fig. 2, S3, S4**). In the Itokawa and DSCO datasets
784 where more of the Cr cap is preserved H fluctuates within the cap (**Fig. S3, S4A-N**). This is
785 likely caused by porosity within the sputter coated capping layer subtly changing the
786 ionization environment. As such, in all APT datasets the majority of this H signal in the Cr
787 layer is likely to be derived from reactions between H from the UHV system and the Cr layer.
788 In the PSCO the increase in H in APT data is mirrored by a complementary increase in OH^+
789 and H_2O^+ ions suggesting at least some contribution to these mass peaks is from reactions
790 between H from the UHV system and the Cr layer (**Fig. S4**). In addition, the sputter coated Cr
791 layer is impure and contains a substantial proportion of O in the form of $CrO^{+ \text{ and } ++}$ ions (**Fig.**
792 **S5A**), as such some of the enrichment in OH^+ and H_2O^+ in the Cr layer is derived from $^{17}O^+$
793 and $^{18}O^+$ isobaric interferences. This also explains the trend in OH and H_2O abundances in
794 the DSCO and Itokawa APT datasets where OH and H_2O decrease in the Cr layer and then
795 plateau at a lower level than the olivine (**Fig. 2, S3, S4A-N**), revealing the presence of
796 residual O in the Cr layer. Cr metal reacts rapidly when exposed to the terrestrial atmosphere
797 to form CrO and as such the presence of O within the sputter coated Cr layer is expected. In
798 two DSCO samples (DSCO1 and DSCO3) **(Fig. 2D-J, S4A-G and 4O-U)** the Cr cap has a
799 lower concentration of Cr relative to DSCO2, PSCO and Itokawa. This is because these two
800 DSCO samples had a substantially thinner Cr layer remaining after FIB preparation meaning
801 the APT analysis only briefly measured the Cr layer prior to transitioning to the DSCO
802 olivine, consequently producing a lower Cr concentration in the Cr capping layer. In the
803 DSCO there is some residual signal from D^+, and D^{2+}, DO^+ D_2O^+ present in the Cr layer, this
804 is due to isobaric interferences with, H_2^+, H_4^+, and $^{18}O^+$ and $^{40}Ca^{++}$ within the sputter coated
805 Cr capping layer and is observed in all APT samples.
806

The effect of the Cr-olivine contact

Cr is enriched within the sputter coated Cr layer as expected. However, in several cases the olivine grain surface is irregular and not normal to the Z-direction of the APT analysis. Thus, the depth profile generated by the wide cylindrical regions of interest in the z-direction of each APT analysis mean the onset of Cr enrichment and hydrous depletions in the DSCO and Itokawa APT data do not perfectly correlate due to the morphology of the grain surface with respect to the region of interest (**Fig. 2, S3, S4, S6**). Extracting a thinner cylinder for our region of interest depth profile reveals that the Cr enrichment and hydrous ion depletions are correlated and relate to the compositional change between the sputter coated Cr and olivine grain surfaces (**Fig. S6**). However, demonstrating this correlation comes at the cost of the counting statistical uncertainty and as such the variations in hydroxide species are less clear (**Fig. S6**). Thus, we chose a cylindrical diameter that acted as a compromise between increasing the amount of data included while preserving the boundary.

In some APT datasets Itokawa 1, Itokawa 2, and DSCO3, there is a minor enrichment trend in H OH and H_2O at the boundary between Olivine and Cr (**Fig. 2, S3, S4)**. This minor enrichment is consistent with variable H and H2O contamination on mineral surfaces sometimes observed and can affect APT datasets to varying degrees[80]. This boundary enrichment in H species is distinct from the secondary enrichment in H species that is 40 nm beneath the surface of the olivine in Itokawa APT data and in deuterium species in DSCO samples (**Fig. 2, S3, S4)** which we interpret as real H or D respectively implanted by the solar wind or irradiation experiments respectively.

Grain size dependence on solar wind derived water abundance.

The contribution of the solar wind derived water to the total water budget of an olivine grain was modelled varying the space weathering rim thickness between 10 nm and 200 nm, which

are typical widths of space weathering surfaces[30,45,50] and varying the grain size between 0-1×10^9 nm. We assume the grain is spherical for simplicity, but it should be noted that the resulting water abundance values will be the minimum value of a particle of that size. We calculated the percentage of the volume of each grain that is affected by space weathering and use the APT data to define the minimum water content present within the space weathered volume to be 1.6 mol. %. We then calculated the total water content for the whole grain (**Data S2**). These were then compared to typical grain sizes for a variety of known extraterrestrial materials to generate **Fig. 3**.

Earth ocean contribution model

The range of possible water contributions from known Solar System water reservoirs to reconcile Earth's oceans was modelled to work out the possible contributions of water from water-rich chondritic asteroids, and solar wind sources that could reproduce Earth's ocean D/H ratio. We assume the contribution of meteorite sized objects to be negligible given the bimodal size distribution of objects falling to the Earth[55-58]. We included bulk anyhydrous ordinary chondrites and enstatite chondrites in our model despite the fact that their overall contribution is likely to be small due to their low water content[10,19,81] which is only compatible with the lowest estimate for the water content of the bulk Earth (**Table 1**), as such we focus on the aqueously altered water-rich CM, CI and CR chondrites[1,16,71,81]. We assumed a D/H ratio of 1.73×10^{-4} [1,4] and water abundance of 2-16 mol. %[71,81] from water rich carbonaceous chondrites (an average of CM (D/H 1.48×10^{-4} [1,16]), CR (D/H 2.57×10^{-4} [1]) and CI (1.68×10^{-4} [1]) based on their current relative abundance in the meteorite collection [CR: 22.3 % CM: 76.6 % and CI: 1.1% [82]], an average D/H ratio of 1.31×10^{-4} [1,4] and water abundance of 0.1-0.8 mol. % for enstatite chondrites, an average D/H ratio of 1.35×10^{-4} [10] and water abundance of 0.1-0.7 mol. % for ordinary chondrites[19] and a D/H ratio of $2\times10^{-}$

857 [7] [4,26] and water abundance of 0.1-1.6 mol. % for solar wind derived water in small particles.
858 The mol. % abundance of water rich chondrites, ordinary chondrites enstatite chondrites and
859 Earth was converted from the wt. % of water in each object (Table 1; 1.6-12.9 %, 0.8-0.54 %
860 and 0.02 % respectively) using the equation below

$$Water_{(Mol.\%)} = \frac{\left(\frac{Water_{(wt.\%)} \times A_N}{Mr_{(H_2O)}}\right) \times 100}{\left[\left(\frac{Water_{(wt.\%)} \times A_N}{Mr_{(H_2O)}}\right) + \left(\frac{(100 - Water_{(wt.\%)}) \times A_N}{Mr_{(bulk)}}\right)\right]}$$

861 Where A_N is Avogadro's constant (6.022×10^{23}), $Mr_{(H2O)}$ is the molecular mass of water (18
862 g/mole), $Mr_{(bulk)}$ is the average molecular mass of the body in question sans water (21.2
863 g/mole for the Bulk Silicate Earth[69], 24 g/mole for carbonaceous chondrites[70], 25.6 g/mol for
864 enstatite chondrites and 24.4 g/mol was used for ordinary chondrites[70]). We modelled the
865 mixture of each of these reservoirs, and our newly defined water budget of space weathered
866 fine-grained particles. By allowing the mass proportion of each reservoir to vary we
867 calculated solutions for this two-component model for each Solar System water source using
868 the equation below.

$$D/H_{(average)} = \left[\frac{\left(Mass\ fraction_{SW} \times SW_{water_{(Mol.\%)}} \times D/H_{SW}\right) + \left((1 - Mass\ fraction_{SW}) \times Asteroid_{water_{(Mol.\%)}} \times D/H_{Asteroid}\right)}{\left(Mass\ fraction_{SW} \times SW_{water_{(Mol.\%)}}\right) + \left((1 - Mass\ fraction_{SW}) \times Asteroid_{water_{(Mol.\%)}}\right)}\right]$$

869 This allowed us to determine mass proportions of each material relative to fine grained solar
870 wind irradiated particles that can reproduce the present-day surface mean ocean water
871 (SMOW) D/H ratio of 1.557×10^{-4} and the Bulk Earth D/H of 1.49×10^{-4} of the Earth[1,17] (**Data**
872 **S3**).

873 Our model is consistent for the assumptions outlined above however, it should be noted that a
874 recent study from Vacher et al., [83] showed that water rich chondrites may have adsorbed

875 substantial amounts of water from the terrestrial atmosphere. This would serve to increase, on
876 average the D/H ratio of water rich chondrites[83] which would in turn increase the contribution
877 of fine-grained solar wind irradiated particulates required. In addition, the total mol. % water
878 of water rich chondrites would be lower once terrestrial adsorbed water was removed[83] which
879 would serve to reduce the contribution of fine-grained solar wind irradiated particles
880 required. However, the amended water abundance values of Vacher et al., [83] are within the
881 range of our current model.

882 In addition, if we only consider the contribution of <10 μm fine grained solar wind irradiated
883 particles that would be sufficiently water-rich (Fig. 3) and that represent 1-10% by mass of
884 the total amount of fine grained extraterrestrial material incident on the Earth today[58]. This
885 would require a larger total contribution of fine-grained materials of up to 90-94 % of the
886 final 0.5 ± 0.25% of Earth's mass during the late veneer (**Fig. S7**). While this greater
887 contribution by mass of fine grained particles is consistent with the contribution of fine
888 grained particles to the mass flux of extraterrestrial materials incident on the Earth throughout
889 its history[38] it is unlikely to be the case that the debris disk was sufficiently dust rich.
890 However, if the particle size distribution of fine-grained materials during the late veneer was
891 more fine grained from that of the present day with a greater proportion by mass of <10 μm
892 particles this would serve to reduce the required fine grained contribution. An increased
893 abundance of fine grained <10 μm grains in the inner solar system is consistent with
894 numerical simulations of IDP grain size variation and distribution that predicts a high
895 proportion of ~5 μm particles in the inner solar system region[42]. In addition, the coarser
896 component of dust particles >10 μm typically comprised of fine-grained porous aggregates
897 e.g. IDPs and fragments of chondritic matrix would contain substantially more solar wind
898 derived water than predicted by our spherical grain model (**Fig. 3**) and would be comparable

in water content to the <10 μm grains. This would also serve to reduce the contribution by mass of fine-grained dust during the late veneer.

The contribution of solar wind derived water may not only be limited to delivery from fine grained dust as during the debris disk stage all materials will experience a radiation rich environment. Thus, all dust produced during this period will incorporate solar wind derived water. Much of this irradiated material will reaccrete onto and/or form primitive asteroids. Consequently, solar wind derived water will become incorporated into the regolith of primitive asteroids as this dust is reaccreted, while many primitive asteroids likely formed from the re-accretion of fine-grained space weathered materials. Therefore, both water rich fine-grained dust and water rich asteroids/asteroid regoliths derived from the (re)accretion of this water rich dust will be produced in the early Solar System. This is consistent with evidence of space weathering and solar wind irradiation of, and incorporation into, chondritic regolith breccias[65,66] and the prevalence of rubble pile asteroids[67].

Data availability statement: The Itokawa particles are on loan to L.D. from JAXA as part of the 5th Announcement of Opportunity. They are currently stored at the University of Glasgow and any remaining fragments and samples will be returned to JAXA on the completion of the project. Because of the nature of APT measurements all atom probe samples detailed in this study have been destroyed. The SCO reference materials produced for this study are stored at Curtin University (PSCO), University of Hawaii (DSCO), and JSC (HeSCO). All data generated or analysed during this study are included in this published article (and its supplementary information files).

Methods references

1 Alexander, C. M. O. D. The origin of inner Solar System water. *Phil Trans Royal Soc* **375**, 20150384 (2017).

2 Marty, B. The origins and concentrations of water, carbon, nitrogen and noble gases on Earth. *Earth & Planet Sci Lett* **313**, 56-66 (2012).

4 Robert, F. The origin of water on Earth. *Sci* **293**, 1056-1058 (2001).

6 Hallis, L. J. *et al.* Evidence for primordial water in Earth's deep mantle. *Sci* **350**, 795-797 (2015).

9 Morbidelli, A. *et al.* Source regions and timescales for the delivery of water to the Earth. *Met & Planet Sci* **35**, 1309-1320 (2000).

10 Piani, L. *et al.* Earth's water may have been inherited from material similar to enstatite chondrite meteorites. *Sci* **369**, 1110-1113 (2020).

16 McCubbin, F. M. & Barnes, J. J. Origin and abundances of H2O in the terrestrial planets, Moon, and asteroids. *Earth & Planet Sci Lett* **526**, 115771 (2019).

17 Lécuyer, C., Gillet, P. & Robert, F. The hydrogen isotope composition of seawater and the global water cycle. *Chem Geol* **145**, 249-261 (1998).

18 Marty, B. *et al.* Origins of volatile elements (H, C, N, noble gases) on Earth and Mars in light of recent results from the ROSETTA cometary mission. *Earth & Planet Sci Lett* **441**, 91-102 (2016).

19 Jin, Z. & Bose, M. New clues to ancient water on Itokawa. *Sci Adv* **5**, eaav8106 (2019).

26 Huss, G., Nagashima, K., Burnett, D., Jurewicz, A. & Olinger, C. A new upper limit on the D/H ratio in the solar wind. *LPI*, 1709 (2012).

28 Lodders, K. Solar system abundances and condensation temperatures of the elements. *Astrophys J* **591**, 1220 (2003).

30 Bradley, J. P. *et al.* Detection of solar wind-produced water in irradiated rims on silicate minerals. *Proc Natl Acad Sci* **111**, 1732-1735 (2014).

38 Pasek, M. & Lauretta, D. Extraterrestrial flux of potentially prebiotic C, N, and P to the early Earth. *Orig Life Evol Bios* **38**, 5-21 (2008).

42 Poppe, A. R. An improved model for interplanetary dust fluxes in the outer Solar System. *Icarus* **264**, 369-386 (2016).

45 Noguchi, T. *et al.* Incipient space weathering observed on the surface of Itokawa dust particles. *Sci* **333**, 1121-1125 (2011).

50 Keller, L. P. & McKay, D. S. The nature and origin of rims on lunar soil grains. *Geochim et Cosmochim Act* **61**, 2331-2341 (1997).

51 Demouchy, S., Jacobsen, S. D., Gaillard, F. & Stern, C. R. Rapid magma ascent recorded by water diffusion profiles in mantle olivine. *Geol* **34**, 429-432 (2006).

55 Zolensky, M. E. *et al.* Mineralogy and petrology of comet 81P/Wild 2 nucleus samples. *Sci* **314**, 1735-1739 (2006).

56 Love, S. & Brownlee, D. A direct measurement of the terrestrial mass accretion rate of cosmic dust. *Sci* **262**, 550-553 (1993).

57 Anders, E. Pre-biotic organic matter from comets and asteroids. *Nat* **342**, 255-257 (1989).

58 Flynn, G., Keller, L., Jacobsen, C. & Wirick, S. An assessment of the amount and types of organic matter contributed to the Earth by interplanetary dust. *Adv Space Res* **33**, 57-66 (2004).

65 Suess, H., Wänke, H. & Wlotzka, F. On the origin of gas-rich meteorites. *Geochim et Cosmochim Act* **28**, 595-607 (1964).

66 Krietsch, D. *et al.* Noble gases in CM carbonaceous chondrites: Effect of parent body aqueous and thermal alteration and cosmic ray exposure ages. *Geochim et Cosmochim Act* (2021).

67 Walsh, K. J. Rubble pile asteroids. *Annual Review of Astronomy and Astrophysics* **56**, 593-624 (2018).

68 Greenberg, J. M. Making a comet nucleus. *Astron & Astrophys* **330**, 375-380 (1998).

69 Szurgot, M. in *Lunar and Planetary Science Conference.* 1536.

70 Anderson, D. L. & Kovach, R. L. The composition of the terrestrial planets. *Earth & Planet Sci Lett* **3**, 19-24 (1967).

71 Garenne, A. *et al.* The abundance and stability of "water" in type 1 and 2 carbonaceous chondrites (CI, CM and CR). *Geochim et Cosmochim Act* **137**, 93-112 (2014).

72 Peslier, A. H., Schönbächler, M., Busemann, H. & Karato, S.-I. Water in the Earth's interior: distribution and origin. *Space Sci Rev* **212**, 743-810 (2017).

73 Dukes, C., Baragiola, R. & McFadden, L. Surface modification of olivine by H+ and He+ bombardment. *J Geophys Res: Planet* **104**, 1865-1872 (1999).

74 Loeffler, M., Dukes, C. & Baragiola, R. Irradiation of olivine by 4 keV He+: Simulation of space weathering by the solar wind. *J Geophys Res: Planet* **114**, E3 (2009).

75 Thompson, K. *et al.* In situ site-specific specimen preparation for atom probe tomography. *Ultramic* **107**, 131-139 (2007).

76 Larson, D. J., Prosa, T., Ulfig, R. M., Geiser, B. P. & Kelly, T. F. Local electrode atom probe tomography. *New York, US: Springer Science* **2** (2013).

77 Lewis, J. B., Isheim, D., Floss, C. & Seidman, D. N. C12/C13-ratio determination in nanodiamonds by atom-probe tomography. *Ultramic* **159**, 248-254 (2015).

78 Meisenkothen, F., Steel, E. B., Prosa, T. J., Henry, K. T. & Kolli, R. P. Effects of detector dead-time on quantitative analyses involving boron and multi-hit detection events in atom probe tomography. *Ultramic* **159**, 101-111 (2015).

79 Stephan, T., Heck, P. R., Isheim, D. & Lewis, J. B. Correction of dead time effects in laser-induced desorption time-of-flight mass spectrometry: Applications in atom probe tomography. *Int J Mass Spectrom* **379**, 46-51 (2015).

80 Kolli, R. P. Controlling residual hydrogen gas in mass spectra during pulsed laser atom probe tomography. *ASCI* **3**, 1-10 (2017).

81 Alexander, C. M. D., McKeegan, K. D. & Altwegg, K. Water reservoirs in small planetary bodies: meteorites, asteroids, and comets. *Space Sci Rev* **214**, 1-47 (2018).

82 LPI. *The Meteoritical Bulletin*, 2020).

83 Vacher, L. G. *et al.* Hydrogen in chondrites: Influence of parent body alteration and atmospheric contamination on primordial components. *Geochim et Cosmochim Act* **281**, 53-66 (2020).

Competing interests: Authors declare no competing interests.

Extended D**ata:**

Extended Data Figures

Fig. S1. Back scatter electron (BSE) and in-beam secondary electron (IbSE) images of the front face of Itokawa particle RA-QD02-0279 and resulting APT specimens. A) BSE image of the front face of Itokawa particle RA-QD02-0279 after Cr coating. B) BSE image of the front face of Itokawa particle RA-QD02-0279 after Ion beam Pt deposition in preparation for sample extraction for APT. The red circles indicate where the APT lift outs were extracted from the wedge. C) IbSE (left) and BSE (right) image of needle (D) half way through annular milling. The Pt protective layer is visible as well as the Cr layer. Annular milling was continued until the Pt was removed but leaving the Cr cap. D-H) IbSE (left) and BSE images (right) of each APT needle the Cr cap is visible at the apex of each tip in the BSE images as well as the Pt weld at the base.

Fig. S2. Back scatter electron (BSE) and in-beam secondary electron (IbSE) images of the back face of Itokawa particle RA-QD02-0279 and resulting APT specimens. A) BSE image of the back face of Itokawa particle RA-QD02-0279 after Cr coating. B) BSE image of the back face of Itokawa particle RA-QD02-0279 after Ion beam Pt deposition in preparation for sample extraction for APT. The red circles indicate where the APT lift outs were extracted from the wedge. C) BSE image of the back face of Itokawa particle RA-QD02-0279 after FIB lift out. D-H) IbSE (left) and BSE images (right) of each APT needle the Cr cap is visible at the apex of each tip in the BSE images as well as the Pt weld at the base.

Fig. S3. APT data from Itoakwa. The APT needles extracted from the front face of **Itokawa particle RA_QD02_0279 shown in** Fig. **S1E (A-C) and** Fig. **S1G (D-F) and in**

from the back face shown in Fig. **S2F (G-I) and** Fig. **S2H (J-L). All data sets initially ran through Cr protective layer (grey spheres) into the olivine surface. A, D, G, and J) APT measurement of the 3D distribution of Cr (grey spheres) and OH (teal spheres) ions through a space weathered surface of this Itokawa particle. B, E, H, and K) APT measurement of the 3D distribution of Cr (grey spheres) and H_2O (blue spheres) ions through a space weathered surface of this Itokawa particle. C, F, I, and L) Concentration of ions in atomic percent (at. %) measured by APT of Itokawa** with depth across the Cr capping layer (Cr, grey shaded region) space weathered rim (SW, blue shaded region) and the non-space weathered olivine (Ol, green shaded region) deeper into the mineral revealing variations in the abundances of Cr (grey line), H (yellow line), OH (green line) and H_2O (blue line) ions**. Line widths have been adjusted to represent the 1 sigma uncertainty and depth profiles are absolute abundances not relative concentrations (**Data S1**).** The boundary between the Cr and SW layer is marked by a vertical dashed red line and the boundary between the SW and Ol layer is marked by a vertical black dashed line.

Fig. S4. APT data from DSCO (A-U) and PSCO (V-X) standards. All data sets initially ran through the Cr protective layer (grey spheres) into the olivine surface. A, H, and O) APT measurements of the 3D distribution of Cr (grey spheres) and D (purple spheres) ions through a DSCO sample. B, I, and P) APT measurements of the 3D distribution of Cr (grey spheres) and D_2 (orange spheres) ions through a DSCO sample. C, J, and Q) APT measurements of the 3D distribution of Cr (grey spheres) and H (yellow spheres) ions through a DSCO sample. D, K, and R) APT measurements of the 3D distribution of Cr (grey spheres) and DO (green spheres) ions through a DSCO sample. E, L, and S) APT measurement of the 3D distribution of Cr (grey spheres) and D_2O (turquoise spheres) ions through a DSCO sample. F, M, and T)

APT measurements of the 3D distribution of Cr (grey spheres) and OH (teal spheres) ions through a DSCO sample. G, N, and U) Concentration of ions in atomic percent (at. %) measured by APT in the DCSO sample with depth across the Cr capping layer (Cr, grey shaded region), Deuterium irradiated rim (DI, blue shaded region) and the non-Deuterium irradiated olivine (Ol, green shaded region) deeper into the mineral revealing the variation in the abundance of Cr (grey line), D (purple line), D_2 (orange line), DO (red line), D_2O (blue line), H (yellow line), and OH (green line) ions. Line widths have been adjusted to represent the 1 sigma uncertainty and depth profiles are absolute abundances not relative concentrations (**Data S1**). The boundary between the Cr and DI layer is marked by a vertical dashed red line and the boundary between the DI and Ol layer is marked by a vertical black dashed line. V) APT measurements of the 3D distribution of Cr (grey spheres) and OH (teal spheres) ions through a PSCO sample. W) APT measurements of the 3D distribution of Cr (grey spheres) and H_2O (blue spheres) ions through a PSCO sample. X) Concentration of ions measured by APT in the PSCO sample with depth across the Cr capping layer (Cr, grey shaded region), into the olivine (Ol, green shaded region). Line widths have been adjusted to represent the 1 sigma uncertainty and depth profiles are absolute abundances not relative concentrations (**Data S1**). The boundary between the Cr and Ol layer is marked by a vertical dashed red and black line.

Fig. S5. Representative APT mass spectra (left) and oxygen series peaks (right). Spectra were produced from regions of interest within: A) the sputter coated Cr layer from **Fig. S3J-L**, B) the bulk olivine of Itokawa from **Fig. S3J-L**, C) the solar wind irradiated rim of Itokawa olivine from **Fig. S3J-L**, D) D-irradiated rim from **Fig. S4H-N**.

Fig. S6. The effect that changing the diameter of the cylindrical region of interest has on the sputter coated Cr and olivine interface and on counting statistics under the peak. A) The 42 nm cylindrical region of interest used to produce the concentration profiles from the APT dataset Itokawa3 **Fig. S3J-L.** B) A 3 nm cylindrical region of interest from the APT dataset Itokawa3. C) Corresponding concentration profiles in atomic percent (at. %) for Cr and H from the 42 nm region of interest and sum Cr and H (including molecular ions) concentration profiles from the 3 nm wide cylinder. We note that the Cr-olivine interface is sharper in the 3 nm wide cylinder but it comes at the expense of the counting statistical uncertainty of the measurement. Line widths have been adjusted to represent the 1 sigma uncertainty and depth profiles are absolute abundances not relative concentrations.

Fig. S7. Diagram of the D/H ratio that results from mixing solar wind irradiated <10 µm fine grained particles and chondritic water reservoirs. The D/H ratio plot is generated by mixing water reservoirs of carbonaceous chondrite (CR[green volume], CI [blue volume], CM [orange volume], Cav [red volume, the average of CR,CI and CMs D/H = 0.000173[[1,16]]; water abundance = 2-16 molecular % per atom[[9]]), ordinary chondrite (purple volume, OC)[19] and enstatite chondrite (brown volume, EC)[10] material, and small space weathered particles, where only particles <10 µm that make up ~10 % of present day fine grained extraterrestrial dust are considered (D/H = 0.0000002[[26]] water abundance = 0.1-1.6 molecular % per atom that can reproduce the SMOW and Bulk Silicate Earth (BSE) D/H ratio[1,17] (horizontal black dashed lines, **Data S3)**. The upper and lower bounds of each field represent the upper and lower limits of the water content within the chondrites and solar wind irradiated particles. The relative mass contributions that span BSE and SMOW D/H ratios indicates the range of potential mixtures of theses extraterrestrial water reservoirs that could generate the present-day D/H of Earth's oceans.

Fig. S8. Operating conditions of the geoscience atom probe (R80). The run number for each sample and sample label are given.

Extended data references

1 Alexander, C. M. O. D. The origin of inner Solar System water. *Phil Trans Royal Soc* **375**, 20150384 (2017).

9 Morbidelli, A. *et al.* Source regions and timescales for the delivery of water to the Earth. *Met & Planet Sci* **35**, 1309-1320 (2000).

10 Piani, L. *et al.* Earth's water may have been inherited from material similar to enstatite chondrite meteorites. *Sci* **369**, 1110-1113 (2020).

16 McCubbin, F. M. & Barnes, J. J. Origin and abundances of H2O in the terrestrial planets, Moon, and asteroids. *Earth & Planet Sci Lett* **526**, 115771 (2019).

17 Lécuyer, C., Gillet, P. & Robert, F. The hydrogen isotope composition of seawater and the global water cycle. *Chem Geol* **145**, 249-261 (1998).

19 Jin, Z. & Bose, M. New clues to ancient water on Itokawa. *Sci Adv* **5**, eaav8106 (2019).

26 Huss, G., Nagashima, K., Burnett, D., Jurewicz, A. & Olinger, C. A new upper limit on the D/H ratio in the solar wind. *LPI*, 1709 (2012).

Title: Solar contributions to Earth's oceans

Authors: Luke Daly*[1,2,3,4], Martin R. Lee[1], Lydia J. Hallis[1], Hope A. Ishii[5], John P. Bradley[5], Phillip. A. Bland[2], David W. Saxey[6], Denis Fougerouse[2,6], William D. A. Rickard[6], Lucy V. Forman[2], Nicholas E. Timms[2], Fred Jourdan[2], Steven M. Reddy[2,6], Tobias Salge[7], Zakaria Quadir[8,9], Evangelos V. Christou[1], Morgan A. Cox[2], Jeffrey A. Aguiar[10,11], Khalid Hattar[12], Anthony Monterrosa[12], Lindsay P. Keller[13], Roy Christoffersen[14], Catherine A. Dukes[15], Mark J. Loeffler[16] and Michelle S. Thompson[17].

Affiliations:

[1]School of Geographical and Earth Sciences, University of Glasgow, Glasgow, G12 8QQ, UK.

[2]Space Science and Technology Centre, School of Earth and Planetary Sciences, Curtin University, GPO Box U1987, Perth, WA 6102, Australia.

[3]Australian Centre for Microscopy and Microanalysis, University of Sydney, Sydney 2006, NSW, Australia.

[4]Department of Materials, University of Oxford, Oxford, OX1 3PH, UK

[5]Hawaii Institute of Geophysics and Planetology, University of Hawai'i at Mānoa, Honolulu, HI, 96822.

[6]Geoscience Atom Probe Facility, Advanced Resource Characterisation Facility, John de Laeter Centre, Curtin University, GPO Box U1987, Perth, WA 6845, Australia.

[7]Imaging and Analysis Centre, Natural History Museum, Cromwell Road, London, SW7 5BD, UK.

[8]School of Civil and Mechanical Engineering, Faculty of Science & Engineering, Curtin University, GPO Box U1987, Perth, WA 6845, Australia.

[9]Microscopy & Microanalysis Facility, John de Laeter Centre, Curtin University, GPO Box U1987, Perth, WA 6845, Australia.

[10]Nuclear Materials Department, Idaho National Laboratory, Idaho Falls, ID USA.

[11]Advanced Technology Center, Lockheed Martin, Palo Alto, CA USA

[12]Sandia National Laboratories, PO Box 5800, Albuquerque, New Mexico, 87185, USA.

[13]Robert M Walker Laboratory for Space Science, Code KR, Astromaterials Research and Exploration Science, NASA Johnson Space Center, Houston, TX, 77058, USA

[14]Jacobs, NASA Johnson Space Center, Mail Code XI3, Houston, TX 77058, USA

[15]Laboratory for Astrophysics and Surface Physics, University of Virginia, Charlottesville, Virginia, 22904, USA

[16]Department of Astronomy and Planetary Science, Northern Arizona University, Flagstaff, Arizona, USA

[17]Department of Earth, Atmospheric and Planetary Sciences, Purdue University, West Lafayette, IN, 47907, USA.

*Correspondence to: luke.daly@glasgow.ac.uk

Summary:

The isotopic composition of water in Earth's oceans is challenging to recreate using a plausible mixture of known extraterrestrial sources such as asteroids - an additional isotopically light reservoir is required. The Sun's solar wind could provide an answer to balancing Earth's water budget. We used atom probe tomography to directly observe an average ~1 molecular percent enrichment in water and hydroxyls in the solar wind irradiated rim of an olivine grain from the S-type asteroid Itokawa. We also experimentally confirm that H irradiation of silicate mineral surfaces produces water molecules. These results suggest that the Itokawa regolith could contain ~20 litres per

m^3 of solar wind derived water and that such water reservoirs are likely ubiquitous on airless worlds throughout our galaxy. The production of this isotopically light water reservoir by solar wind implantation into fine grained silicates may have been a particularly important process in the early Solar System, potentially providing a means to recreate Earth's current, water-isotope ratios.

Main Text:

The origin of Earth's water and volatile budget is a topic of considerable debate in planetary science[1-10]. Most current dynamical models of Earth's formation assume that the majority of Earth's water and other volatiles was added later from an exogenous source[1-4]. That volatile source shared a common parent population with C-type asteroids, that is likely located in the Jupiter-Saturn region and beyond[11-14]. C-Type asteroids are thought to be the parent bodies of carbonaceous (C) chondrite meteorites as they exhibit similar reflectance spectra, in particular the CRs, CMs and CIs[15], which can contain up to 10 weight percent (wt. %) H_2O **(Table 1)**[9]. Although the D/H isotope ratios of C-chondrite meteorites are a closer fit to the Earth than to comets or other meteorite types, with CMs being a particularly close match **(Table 1)**[2,16], the Earth's mantle and Standard Mean Ocean Water (SMOW) are lighter in D/H[17] than the average of CI-, CR- and CM-chondrite groups [e.g., [1,16,18] **Table 1**]. Given the diversity of water rich C-chondrites in the meteorite record, it is unlikely that CM-like asteroids alone delivered all of Earth's water. Thus, as they are the most water-rich meteorites [9], the CIs, CRs and CMs are believed to represent the majority of Earth's chondritic water component. Although recent studies of nominally anhydrous minerals from enstatite chondrites[10] and Itokawa particles[19] suggests that these materials may be more water-rich than previously thought, they only contain sufficient water for the lowest estimate of Earth's water budget (**Table 1**). D/H ratios of the Earth's deep mantle are even lighter than SMOW **(Table 1)**[2]; recent analysis of volcanically exhumed material indicate that a component of

isotopically-light, solar-like D/H may be extant in the primitive mantle **(Table 1)**[6]. In addition, the bulk D/H ratio of the Earth may have increased from its initial value over the last 4.5 Ga potentially due to a preferential loss of the lighter hydrogen isotope to space[20]. However, increasing the D/H ratio via this mechanism is challenging to reconcile with extraterrestrial delivery of other isotope systems from C-type material e.g. Nitrogen[3]. Nevertheless, the volatile isotopic composition of the Earth is an enigma and it is likely that at least one other light isotope reservoir must have contributed to our planet's water budget - e.g., the Sun and/or the solar nebula.

The Sun could provide this additional reservoir, as it is isotopically light compared to SMOW and the bulk Earth **(Table 1)**[4]. It has been suggested that H adsorption onto mineral grain surfaces in the nebula[21] or dissolution of nebular H_2 into Earth's magma ocean[7,22] could have contributed a solar nebula D/H component. However, there are substantial challenges to this model[3] and the abundance of H deliverable by this mechanism is unconstrained and would only be a contributing factor while the gaseous nebula is present. A late veneer of the final 0.5 ± 0.25 % of Earth's mass[23-25], post core formation and after the gas disk had dissipated is likely to have contributed some of Earth's water from a predominantly chondritic source[11-14], but may still require a light D/H reservoir.

Intriguingly, volatile isotope ratios of hydrogen from the solar wind (e.g. $D/H = 2\times10^{-7}$ **(Table 1)**[26]), and the surfaces of materials that have been irradiated by solar wind, such as the samples recovered from NASA's GENESIS mission[27], have D/H isotope ratios consistent with the protosun and protosolar nebula[26,27]. The composition of the solar photosphere, and by extension the solar wind, is 96 % H and 4 % He, with the remaining ions comprised of all elements in their solar abundance ratios[28,29].

It has been demonstrated by observation and experimentation that solar wind irradiation of rocky materials results in a reaction between H ions and silicate minerals to produce OH and

98 water[5,30-34]. These molecules may become trapped in the 20-200 nm thick damage layer
99 induced by solar wind irradiation and other space weathering processes[30]. This phenomenon
100 could explain why the regoliths of airless worlds such as the Moon, which were once thought
101 to be anhydrous, contain several percent water[35-37]. Implantation of Solar H may also explain
102 why nominally anhydrous minerals in asteroids have water abundances of several hundred
103 parts per million[10,19] by weight. Clear evidence for these reactions also comes from the
104 detection of OH bonds and inferred water contents of up to 1 mol. % (where mol.% is
105 equivalent to the percentage of water molecules [sum total of H, OH and H_2O ions per 100
106 atoms of a material see **methods**), in the solar wind irradiated surfaces of interplanetary dust
107 particles (IDPs), as well as the production of water in minerals during laboratory space
108 weathering experiments[30,33]. These lines of evidence hint that a volatile reservoir isotopically
109 similar to the solar wind may have been present in the Solar System and contributed to
110 Earth's oceans. One potentially important source of such water, whose contribution has yet to
111 be quantitatively evaluated, is the regolith of silicate-rich asteroids and other fine-grained
112 extraterrestrial materials such as IDPs and the matrix of primitive chondrite meteorite. Such
113 materials comprise ~99% of the present day extraterrestrial mass flux[38]; they were produced
114 in high quantities through a variety of mechanisms including during impacts between
115 planetesimals, active outgassing or disruptive outbursts from comets and asteroids
116 bombardment by and collisions between IDPs, in the radiation-rich debris disk stage of a
117 protoplanetary disk[39-42], and so also during the late veneer stage of accretion of the terrestrial
118 planets.

119 Atom probe tomography (APT) is a quantitative analytical technique capable of measuring
120 the abundance of water and OH molecules within minerals in three dimensions at sub-
121 nanometre resolution[43]. We utilized APT to measure water abundances of space weathered
122 surfaces on both sides of a particle from the asteroid Itokawa (RA-QD02_0279) (**methods**

Fig. 1, S1, S2, S6-8) that was returned to Earth by JAXA's Hayabusa mission in 2011[44]. Our Itokawa APT data (**Fig. 2, S3, S5A-C**) are supported by results from analyses of the same particle by scanning electron microscopy (SEM) (**Fig. 1A-B, S1-2**), and transmission electron microscopy (TEM) (**Fig. 1C-E**). In addition, APT measurements of three experiments using San Carlos olivine (SCO) standard reference materials support this work. One pristine SCO sample was exposed to the laboratory atmosphere (PSCO), one was irradiated with He^+ (HeSCO) at 4 keV, and a third was irradiated with D^+ (DSCO) at 1 and 10 keV (**Fig 2D-J, S4, S5D and methods**). The energy used during the D^+ and He^+ irradiation experiments is consistent with that of the solar wind.

SEM images of the Itokawa grain show that its surface has an angular, pristine appearance and is free of micrometeorite impact craters (**Fig. 1A-B, S1-2**). TEM images of the particle indicate that it has a 40-50 nm thick solar wind irradiated rim that is crystalline and exhibits slight variations in density (**Fig. 1C-E**). The space weathered rim was sensitive to irradiation by the electron beam, resulting in a change in contrast, relative to the rest of the grain, which could be due to its volatile enrichment. No Fe nanoparticles were observed (**Fig. 1C-E**) in contrast to reports from other Itokawa grains[45] and APT analyses of Lunar ilmenite[46]. The properties of the solar wind irradiated surface and rim of this grain indicate that its space weathering features could be immature, maybe because it was exposed for a shorter period than other previously characterized space weathered Itokawa grains[45].

APT results from the Itokawa grain reveal that OH and water are enriched in the rims on both sides of the particle by 0.1-1.6 ± 0.05 molecular percent above background (Mol. %; where mol.% is equivalent to the percentage of water molecules [sum total of H, OH and H_2O ions per 100 atoms of a material see **methods**) (**Fig. 2A-C, S3, S5, and methods**). The depth of water implantation (40-180 nm) is consistent with Monte Carlo simulations of the penetration

147 depth of solar wind derived H^+ into silicate minerals at heliocentric distances of Itokawa[47],
148 and with our TEM observations (**Fig 1C-E**).

149 APT data revealed that there was no OH or H_2O enrichment in the near surface profile of the
150 PSCO grains, indicating that the signal in the Itokawa particle is not an artifact of sample
151 handling or laboratory analysis (**Fig S4V-X**). In contrast, the outermost 50 nm of the DSCO
152 sample is enriched with respect to D_2, DO and D_2O (**Fig. 2D-J, S4A-U, S5D**). While this rim
153 is similar in thickness to the space weathered profile of Itokawa, importantly no H was
154 generated by laboratory irradiation, and a substantially lower H and OH signal was observed
155 across the DSCO rim relative to the unirradiated bulk olivine portion of the DSCO sample
156 (**Fig 2D-J, S4A-U, S5D**). This DSCO result further confirms that heavy water can be
157 generated by D irradiation of silicate mineral surfaces, and therefore, H irradiation would
158 similarly generate water[5,30-34]. Additionally, the absence of H and OH in the rim of the D-
159 irradiated grain (**Fig. 2D-J, S4A-U, S5**) indicates that isotopic exchange of an irradiated grain
160 surface with the terrestrial atmosphere is minimal, at least over curatorial timescales. Thus,
161 APT results acquired from the SCO standard materials confirm that the Itokawa results are
162 not a consequence of sample preparation or terrestrial contamination and therefore must be
163 due to extraterrestrial processes, specifically solar wind implantation of volatiles (**methods,**
164 **Fig. 2D-J, S4, S5D**).

165 Despite the immature space weathering of the Itokawa grain (**Fig. 1, S1-2, [**[45]]), we observe
166 an implanted water enrichment (0.1-1.6 ± 0.05 mol. %) in its rims (**Fig. 2A-C, S3, S5A-C**).
167 These water abundances are similar to those detected in space weathered rims of a similar
168 thickness on the surfaces of silicate grains from IDPs[30]. Thus, comparable water abundances
169 have now been determined for two solar wind irradiated materials using two different
170 techniques, giving confidence in the enrichment level provided by both sets of measurements.
171 This measured water enrichment is interpreted as the 'saturated' value where solar wind

172 implantation is in equilibrium with volatile loss in the space environment through solar
173 heating and prolonged (~8 Ma for Itokawa[48]) exposure to a vacuum[49]. Thus, using this water
174 enrichment value (0.1-1.6 ± 0.05 mol. %) and assuming a space weathered rim thicknesses of
175 40-200 nm[30,47,50] for olivine and other silicate minerals, the overall water abundance imbibed
176 into olivine grains of various sizes can be calculated (**Fig. 3, methods**). A space weathered
177 spherical particle with a diameter of 100 μm, typical for most Itokawa regolith grains[44,45,47],
178 would contain ~0.01 mol. % solar wind derived water (**Fig. 3**). Assuming that water
179 enrichment by the solar wind is consistent between grains and minerals that comprise the
180 regolith of Itokawa, every 1 m^3 of Itokawa regolith could contain up to ~20 litres of solar
181 wind derived water. As such, solar wind irradiated silicate minerals may represent a
182 substantial renewable source of water on airless worlds throughout the galaxy.

183 The abundance of water within a particular grain will depend its indigenous water
184 constrained by its mineralogy, and source, and the abundance of solar wind derived water
185 which is dependent on the particles grain size and shape. Most terrestrial olivine contains
186 ~0.001-0.01 mol. % water (e.g. [51]). Itokawa regolith and ordinary chondrite silicates may be
187 more water-rich throughout, where pyroxene grains from Itokawa, and pyroxene and olivine
188 grains within ordinary chondrites and chondrule glasses within enstatite chondrites have
189 measured water contents of 0.016-0.0998 mol. %[[10,19]]. Thus, assuming spherical particles
190 >100 μm in size the solar wind contribution to their overall water budget would be < 50 %.
191 Where ~100 μm in diameter, the solar wind derived water of a particle would represent at
192 least half its total water budget, producing a nominally water-poor particle with an isotopic
193 signal between the heavier chondritic values[1,16] and lighter solar values[4,27-29]. However, the
194 solar wind derived component would constitute 0.1-1.6 mol. % water in particles <10 μm in
195 diameter (**Fig. 3**), thus close to 100% of the water present in the grain.

196 Particle sizes of <10 μm are typical for the matrices of primitive chondritic meteorites[52,53],
197 IDPs[54], and cometary fragments from Wild 2 recovered by the Stardust mission[55]. At the
198 present-day, ~30,000 tons of small particles (submicrometre-mm with a peak at 200 μm)
199 thought to originate from comets, asteroids and IDPs fall to Earth each year[56-58] representing
200 99.9% of the annual delivery of extraterrestrial matter[38]; IDPs alone contribute ~1% of
201 Earth's current annual extraterrestrial input[58]. In addition, coarse >100 μm highly porous
202 aggregates such as IDPs[54] and fragments of chondritic matrix[52,53] that have a larger surface
203 area to volume ratio would also be substantially enriched in solar wind derived water and
204 may be comparable in solar wind derived water contents to <200 nm isolated grains.
205 Therefore, isolated grains in interplanetary space of similar size, irradiated by the solar wind,
206 could represent a significant source of isotopically light water in the Solar System.

207 Assuming that this particle size distribution is also representative of the debris disk stage of
208 Solar System formation, following the dissipation of the solar nebula where the disk would
209 have become transparent, then fine grained and/or porous particles in the IDP-chondritic
210 matrix size range, that are isotopically light and water-rich, may have been accreted alongside
211 planetesimal sized objects during the late veneer to contribute the final 0.5 ± 0.25 % of
212 Earth's mass. Since many of these particles are nano-composites of (organic) carbon and
213 silicate minerals[30,59], solar wind production of water at their surfaces may have been
214 accompanied by diversification of molecular chemistry. However, for fine grained materials
215 irradiated by the solar wind to have contributed significantly to the Earth's late veneer, dust
216 generation at this time period must have been greater than at the present day. Indeed,
217 observations of dusty debris disks in our Galaxy by WISE indicate that between 10^{-1} and 10^{-4}
218 Earth masses is present as micrometre sized dust [60]. Similar dust abundances present during
219 this stage of our own Solar System's formation. The dust would then have been accreted
220 alongside large chondritic asteroids. Very little dust, particularly fine grained materials, will

have remained in the protoplanetary disk once the nebular gas had dissipated[61]. However, substantial amounts of dust are observed in current debris-disks around nascent planetary systems[41] that likely formed by giant impacts e.g. [39-41], collisional cascades between ~100 km size bodies resulting in runaway collisions between progressively smaller asteroids and resulting in their complete disaggregation into micrometre sized dust[60], as well as active outgassing and disruptive outbursts from primitive asteroids and comets[42]. In addition, numerical modelling of the evolution of IDP size suggests that fine grained dust in the ~5 μm size range dominates the mass fraction of dust in the inner solar system at the expense of larger IDPs[42]. This would provide an abundance of fine grained particles implanted with a major component of solar wind derived water. Thus the abundance of fine grained particles like IDPs during this time period are expected to be orders of magnitude greater than the present day[56,62]. This newly formed dust would subsequently have been exposed to the solar wind to produce water before it was (re)accreted by the terrestrial planets and asteroids. An additional consideration is that during the debris disk stage of the early Solar System, particles would have experienced much more intense solar wind irradiation than at the present-day because, while the early Sun was much fainter during its formation, the solar wind flux was higher and more energetic[63,64]. This enhanced solar wind flux would be particularly significant during the energetic T-Tauri stage of our Sun[56]. Therefore, exposed small particles would have accumulated more water than at the present-day by virtue of elevated OH forming reactions with solar wind H ions and a thicker space weathered rim. Furthermore, the noble gas abundance and microstructural features of components within primitive chondrites that are consistent with paleo space weathering indicate that many primitive bodies formed from materials that experienced solar wind irradiation during the debris disk stage[65,66]. Many chondrites are breccias, while many asteroids are rubble piles[67] indicating that primitive asteroids may have experienced one, if not several, cycles of

246 accretion, disruption and re-accretion and thus would have incorporated solar wind derived
247 water as they reaccreted fine grained materials that had been exposed to the radiation rich
248 environment of the early Solar System. Thus, both fine grained dust, as well as the bodies
249 onto which this dust accreted, contain significant solar wind generated water.

250 We have modeled the abundance and isotopic composition of water in four reservoirs:
251 enstatite chondrites, water-rich chondrites (CM, CR and CI), ordinary chondrites and solar
252 wind (**methods**). If only the average D/H ratio and water abundance of water-rich chondrite
253 and solar wind contributions are considered, an addition of water from solar wind irradiated
254 small particles of between 52-76% by mass is required alongside water-rich chondrites to
255 produce Earth's D/H ratio (**Fig. 4**) during the late veneer. However, if only CM meteorites
256 are considered, a 0% contribution by mass of solar wind derived water is required (**Fig. 4**).
257 The water reservoir derived from solar wind irradiated fine grained particles and their
258 calculated mass contribution to Earth during the late veneer, is substantially lower than the
259 present-day (99% by mass) and past mass contribution of small particles relative to larger
260 bodies over most of Earth's history[38] but may be consistent with the relative abundance of
261 fine grained dust and larger planetesimals during the late veneer. In addition, our model
262 predicts that contributions from enstatite chondrites and ordinary chondrites during late-stage
263 accretion of the Earth would reduce the quantity of small solar wind irradiated particles
264 required to account for terrestrial D/H ratios. However, the water-poor nature of these
265 chondrites would still necessitate some contribution from fine grained particles that have
266 been implanted with water by the solar wind for all but the lowest estimate of the water
267 abundance of the Bulk Earth (**Table 1**). In this minimal terrestrial water scenario, no Solar
268 wind derived water is required but a 96-94% contribution of enstatite or ordinary chondrite
269 like material is required to provide the low D/H water contribution to Earth's water budget.

Our quantification of the magnitude of water enrichment in solar wind irradiated grains implies that accretion of a reservoir of volatile-rich small particles during the late veneer could reconcile the D/H isotopic composition of Earth's oceans. A contribution of water from solar wind irradiated small particles during the latter stages of Earth's accretion may be a key factor in reconciling the D/H ratio of Earth's final water budget. In addition, the continuous flux of small particles over Earth's history could help to reduce any isotopic fractionation of Earth's oceans by replacing any of the light isotopes of H that could be lost to space over time (e.g. [20]).

Main references

1 Alexander, C. M. O. D. The origin of inner Solar System water. *Phil Trans Royal Soc* **375**, 20150384 (2017).

2 Marty, B. The origins and concentrations of water, carbon, nitrogen and noble gases on Earth. *Earth & Planet Sci Lett* **313**, 56-66 (2012).

3 Meech, K. & Raymond, S. N. Origin of Earth's Water: Sources and Constraints. *Planet Astrobio*, 325 (2020).

4 Robert, F. The origin of water on Earth. *Sci* **293**, 1056-1058 (2001).

5 Greenwood, J. P. *et al.* Hydrogen isotope ratios in lunar rocks indicate delivery of cometary water to the Moon. *Nat Geo* **4**, 79-82 (2011).

6 Hallis, L. J. *et al.* Evidence for primordial water in Earth's deep mantle. *Sci* **350**, 795-797 (2015).

7 Ikoma, M. & Genda, H. Constraints on the mass of a habitable planet with water of nebular origin. *Astrophys J* **648**, 696 (2006).

8 Morbidelli, A. *et al.* Fossilized condensation lines in the Solar System protoplanetary disk. *Icarus* **267**, 368-376 (2016).

9 Morbidelli, A. *et al.* Source regions and timescales for the delivery of water to the Earth. *Met & Planet Sci* **35**, 1309-1320 (2000).

10 Piani, L. *et al.* Earth's water may have been inherited from material similar to enstatite chondrite meteorites. *Sci* **369**, 1110-1113 (2020).

11 O'Brien, D. P., Walsh, K. J., Morbidelli, A., Raymond, S. N. & Mandell, A. M. Water delivery and giant impacts in the 'Grand Tack'scenario. *Icarus* **239**, 74-84 (2014).

12 Raymond, S. N. & Izidoro, A. The empty primordial asteroid belt. *Sci Adv* **3**, e1701138 (2017).

13 Raymond, S. N., Quinn, T. & Lunine, J. I. High-resolution simulations of the final assembly of Earth-like planets I. Terrestrial accretion and dynamics. *Icarus* **183**, 265-282 (2006).

14 Walsh, K. J., Morbidelli, A., Raymond, S. N., O'Brien, D. P. & Mandell, A. M. A low mass for Mars from Jupiter's early gas-driven migration. *Nat* **475**, 206-209 (2011).

15 Bates, H., King, A., Donaldson Hanna, K., Bowles, N. & Russell, S. Linking mineralogy and spectroscopy of highly aqueously altered CM and CI carbonaceous chondrites in preparation for primitive asteroid sample return. *Met & Planet Sci* **55**, 77-101 (2020).

16 McCubbin, F. M. & Barnes, J. J. Origin and abundances of H2O in the terrestrial planets, Moon, and asteroids. *Earth & Planet Sci Lett* **526**, 115771 (2019).

17 Lécuyer, C., Gillet, P. & Robert, F. The hydrogen isotope composition of seawater and the global water cycle. *Chem Geol* **145**, 249-261 (1998).

18 Marty, B. *et al.* Origins of volatile elements (H, C, N, noble gases) on Earth and Mars in light of recent results from the ROSETTA cometary mission. *Earth & Planet Sci Lett* **441**, 91-102 (2016).

19 Jin, Z. & Bose, M. New clues to ancient water on Itokawa. *Sci Adv* **5**, eaav8106 (2019).

20 Genda, H. & Ikoma, M. Origin of the ocean on the Earth: early evolution of water D/H in a hydrogen-rich atmosphere. *Icarus* **194**, 42-52 (2008).

21 Asaduzzaman, A., Muralidharan, K. & Ganguly, J. Incorporation of water into olivine during nebular condensation: Insights from density functional theory and thermodynamics, and implications for phyllosilicate formation and terrestrial water inventory. *Met & Planet Sci* **50**, 578-589 (2015).

22 Sasaki, S. The primary solar-type atmosphere surrounding the accreting Earth: H 2 O-induced high surface temperature. *LPI*, 195-209 (1990).

23 Dauphas, N. & Marty, B. Inference on the nature and the mass of Earth's late veneer from noble metals and gases. *J Geophys Res: Planet* **107**, 12-11-12-17 (2002).

24 Day, J. M., Pearson, D. G. & Taylor, L. A. Highly siderophile element constraints on accretion and differentiation of the Earth-Moon system. *Sci* **315**, 217-219 (2007).

25 Walker, R. J. Highly siderophile elements in the Earth, Moon and Mars: update and implications for planetary accretion and differentiation. *Geochemistry* **69**, 101-125 (2009).

26 Huss, G., Nagashima, K., Burnett, D., Jurewicz, A. & Olinger, C. A new upper limit on the D/H ratio in the solar wind. *LPI*, 1709 (2012).

27 Geiss, J. & Gloeckler, G. in *Primordial Nuclei and their Galactic evolution* 239-250 (Springer, 1998).

28 Lodders, K. Solar system abundances and condensation temperatures of the elements. *Astrophys J* **591**, 1220 (2003).

29 Marty, B., Chaussidon, M., Wiens, R., Jurewicz, A. & Burnett, D. A 15N-poor isotopic composition for the solar system as shown by Genesis solar wind samples. *Sci* **332**, 1533-1536 (2011).

30 Bradley, J. P. *et al.* Detection of solar wind-produced water in irradiated rims on silicate minerals. *Proc Natl Acad Sci* **111**, 1732-1735 (2014).

31 Ichimura, A., Zent, A., Quinn, R., Sanchez, M. & Taylor, L. Hydroxyl (OH) production on airless planetary bodies: Evidence from H+/D+ ion-beam experiments. *Earth & Planet Sci Lett* **345**, 90-94 (2012).

32 Liu, Y. *et al.* Direct measurement of hydroxyl in the lunar regolith and the origin of lunar surface water. *Nat Geo* **5**, 779-782 (2012).

33 Lucey, P. *et al.* Understanding the lunar surface and space-Moon interactions. *Rev Min and geochem* **60**, 83-219 (2006).

34 Zhu, C. *et al.* Untangling the formation and liberation of water in the lunar regolith. *Proc Natl Acad Sci* **116**, 11165-11170 (2019).

35 Bandfield, J. L., Poston, M. J., Klima, R. L. & Edwards, C. S. Widespread distribution of OH/H2O on the lunar surface inferred from spectral data. *Nat Geo* **11**, 173-177 (2018).

36 Pieters, C. M. *et al.* Character and spatial distribution of OH/H2O on the surface of the Moon seen by M3 on Chandrayaan-1. *Sci* **326**, 568-572 (2009).

37 Sunshine, J. M. *et al.* Temporal and spatial variability of lunar hydration as observed by the Deep Impact spacecraft. *Sci* **326**, 565-568 (2009).

38 Pasek, M. & Lauretta, D. Extraterrestrial flux of potentially prebiotic C, N, and P to the early Earth. *Orig Life Evol Bios* **38**, 5-21 (2008).

39 Canup, R. M. Simulations of a late lunar-forming impact. *Icarus* **168**, 433-456 (2004).

365 40 Krot, A. N., Amelin, Y., Cassen, P. & Meibom, A. Young chondrules in CB
366 chondrites from a giant impact in the early Solar System. *Nat* **436**, 989-992 (2005).
367 41 MacGregor, M. A. *et al.* Constraints on planetesimal collision models in debris disks.
368 *Astrophys J* **823**, 79 (2016).
369 42 Poppe, A. R. An improved model for interplanetary dust fluxes in the outer Solar
370 System. *Icarus* **264**, 369-386 (2016).
371 43 Reddy, S. M. *et al.* Atom Probe Tomography: Development and Application to the
372 Geosciences. *GGR* **44**, 5-50 (2020).
373 44 Nakamura, T. *et al.* Itokawa dust particles: a direct link between S-type asteroids and
374 ordinary chondrites. *Sci* **333**, 1113-1116 (2011).
375 45 Noguchi, T. *et al.* Incipient space weathering observed on the surface of Itokawa dust
376 particles. *Sci* **333**, 1121-1125 (2011).
377 46 Greer, J. *et al.* Atom probe tomography of space□weathered lunar ilmenite grain
378 surfaces. *Met & Planet Sci* **55**, 426-440 (2020).
379 47 Noguchi, T. *et al.* Space weathered rims found on the surfaces of the Itokawa dust
380 particles. *Met & Planet Sci* **49**, 188-214 (2014).
381 48 Nagao, K. *et al.* Irradiation history of Itokawa regolith material deduced from noble
382 gases in the Hayabusa samples. *Sci* **333**, 1128-1131 (2011).
383 49 Crider, D. H. & Vondrak, R. Hydrogen migration to the lunar poles by solar wind
384 bombardment of the Moon. *Adv Space Res* **30**, 1869-1874 (2002).
385 50 Keller, L. P. & McKay, D. S. The nature and origin of rims on lunar soil grains.
386 *Geochim et Cosmochim Act* **61**, 2331-2341 (1997).
387 51 Demouchy, S., Jacobsen, S. D., Gaillard, F. & Stern, C. R. Rapid magma ascent
388 recorded by water diffusion profiles in mantle olivine. *Geol* **34**, 429-432 (2006).

52 Nuth III, J. A., Brearley, A. J. & Scott, E. R. in *Chondrites and the protoplanetary disk.* 675.

53 Bland, P. A. *et al.* Why aqueous alteration in asteroids was isochemical: High porosity≠ high permeability. *Earth & Planet Sci Lett* **287**, 559-568 (2009).

54 Rietmeijer, F. J. Size distributions in two porous chondritic micrometeorites. *Earth & Planet Sci Lett* **117**, 609-617 (1993).

55 Zolensky, M. E. *et al.* Mineralogy and petrology of comet 81P/Wild 2 nucleus samples. *Sci* **314**, 1735-1739 (2006).

56 Love, S. & Brownlee, D. A direct measurement of the terrestrial mass accretion rate of cosmic dust. *Sci* **262**, 550-553 (1993).

57 Anders, E. Pre-biotic organic matter from comets and asteroids. *Nat* **342**, 255-257 (1989).

58 Flynn, G., Keller, L., Jacobsen, C. & Wirick, S. An assessment of the amount and types of organic matter contributed to the Earth by interplanetary dust. *Adv Space Res* **33**, 57-66 (2004).

59 Ishii, H. A. *et al.* Multiple generations of grain aggregation in different environments preceded solar system body formation. *Proc Natl Acad Sci* **115**, 6608-6613 (2018).

60 Vican, L. & Schneider, A. The evolution of dusty Debris disks around solar type stars. *Astrophys J* **780**, 154 (2013).

61 Wyatt, M. The insignificance of PR drag in detectable extrasolar planetesimal belts. *Astron & Astrophys* **433**, 1007-1012 (2005).

62 Nesvorný, D. *et al.* Cometary origin of the zodiacal cloud and carbonaceous micrometeorites. Implications for hot debris disks. *Astrophys J* **713**, 816 (2010).

63 Ayres, T. R. Evolution of the solar ionizing flux. *J Geophys Res: Planet* **102**, 1641-1651 (1997).

64 Kass, D. & Yung, Y. L. Loss of atmosphere from Mars due to solar wind-induced sputtering. *Sci* **268**, 697-699 (1995).

65 Suess, H., Wänke, H. & Wlotzka, F. On the origin of gas-rich meteorites. *Geochim et Cosmochim Act* **28**, 595-607 (1964).

66 Krietsch, D. *et al.* Noble gases in CM carbonaceous chondrites: Effect of parent body aqueous and thermal alteration and cosmic ray exposure ages. *Geochim et Cosmochim Act* (2021).

67 Walsh, K. J. Rubble pile asteroids. *Annual Review of Astronomy and Astrophysics* **56**, 593-624 (2018).

Acknowledgments: The authors would like to thank Dr. Martin Suttle for the preparation and loan of the mounting rod, and Dr. Ryan Ickert for providing access to the clean lab facility at the Scottish Universities Environmental Research Centre to mount the Itokawa particles and Ms Rasika Mahajan for providing a suitably fine-grained basaltic fragments to practice on. L.D. would also like to thank NASA JSC and the Lunar and Planetary Institute for the training received at the 4th training in the extraterrestrial sample handling course. The authors would also like to thank the three anonymous reviewers and editor Dr. Marios Karouzos for their thoughtful, insightful and constructive comments that vastly improved this manuscript. **Funding:** This work was funded by the UK STFC consortium grant, and UAE seed grant awarded to MRL, as well as a SAGES small grant awarded to LD. HI and JB were partially supported by the NASA LARS Program (80NSSC18K0936). This work was partially supported in part through the INL Laboratory Directed Research & Development (LDRD) Program under DOE Idaho Operations Office Contract DE-AC07-05ID145142 that supported JAA. This work was conducted within the Geoscience Atom Probe Facility at Curtin University, which is part of the Advanced Resource Characterization Facility (ARCF).

The Advanced Resource Characterization Facility is being developed under the auspices of the National Resource Sciences Precinct – a collaboration between CSIRO, Curtin University and The University of Western Australia – and is supported by the Science and Industry Endowment Fund (SIEF RI13-01). The authors acknowledge the use of Curtin University's Microscopy and Microanalysis Facility, whose instrumentation has been partially funded by the University, State and Commonwealth Governments. This work was performed, in part, at the Center for Integrated Nanotechnologies, an Office of Science User Facility operated for the U.S. Department of Energy (DOE) Office of Science. Sandia National Laboratories is a multi-mission laboratory managed and operated by National Technology and Engineering Solutions of Sandia, LLC, a wholly owned subsidiary of Honeywell International, Inc., for the U.S. DOE's National Nuclear Security Administration under contract DE-NA-0003525. The views expressed in the article do not necessarily represent the views of the U.S. DOE or the United States Government.

Author contributions: LD conceived the project with input from MRL. Itokawa sample handling and mounting was conducted by MAC and LD. Itokawa SEM analysis was conducted by TS MAC and LD. HI and JB prepared the polished SC olivine on Ta for D_2^+ irradiation. JA arranged and advised instrumentation for D_2^+ irradiation. KH and AM performed D_2^+ irradiations. LPK, RC, and MST prepared the polished SC olivine for He^+ irradiation and CAD and MJL conducted the irradiation. LD and SMR prepared the polished SC olivine and conducted the laboratory exposure. Cr coating was undertaken by WDAR, DF and LD FIB preparations for TEM and APT was undertaken by LD, DF, WDAR. TEM work was conducted by ZA, LD and WDAR. APT analysis was undertaken by DS, DF and LD. Interpretation of the results was conducted by LD, PAB, LVF, MRL, LJH, NET, FJ, DWS and DF. LD, HI, and WDAR, wrote the methods. LD wrote the manuscript with input from all co-authors.

Main Figure legends

Fig. 1. SEM and TEM analyses of the space weathered (SW) surface of Itokawa particle RA_QD02_0279. (A) and (B) Secondary electron images of the front and rear surfaces, respectively, of the particle. Boxes indicate extraction locations of TEM (red) and APT (orange) samples. (C) TEM EDS Fe Kα X-ray map of the grain surface. Fe-nanoparticles are absent, and subtle variations in Fe X-ray signal are due to contrasting density through the rim, not compositional variations. The protective Cr coat, space weathered rim (SW) and unweathered olivine (Ol) are labelled. (D) Bright-field TEM image of the outermost part of the olivine grain and Cr coat. The 50 nm thick SW rim is readily apparent beneath the grain surface and is delineated by two dashed white lines. The patchy contrast of the rim indicates variations in the intensity of electron scattering and density, but not in composition. (E) High Angle Annular Dark Field (HAADF) TEM image of the protective Cr coat, SW rim and unweathered olivine (Ol). Lattice fringes with a 0.35 nm spacing, probably {120 planes (yellow), extend through the SW rim indicating that it is at least in part, crystalline.

Fig. 2. Representative APT data from Itokawa particle RA_QD02_0279 (A-C) and DSCO (D-J). All data sets extend from the Cr protective layer (grey spheres) through the space weathered surface and into unweathered olivine. (A) APT measurement of the 3D distribution of Cr (grey spheres) and OH ions (teal spheres). (B) APT measurement of the 3D distribution of Cr and H_2O ions (blue spheres). (C) Concentration of ions in atomic percent (at. %; number of atoms per 100 atoms) with depth across the Cr capping layer (Cr, grey shaded region) space weathered rim (SW, blue shaded region) and the non-space weathered olivine (Ol, green shaded region) deeper into the mineral revealing variations in the

488 abundances of Cr (grey line), H (yellow line), OH (green line) and H_2O (blue line) ions. Line
489 widths have been adjusted to represent the 1 sigma uncertainty and depth profiles are absolute
490 abundances not relative concentrations (**Data S1**). The boundary between the Cr and SW
491 layer is marked by a vertical dashed red line and the boundary between the SW and Ol layer
492 is marked by a vertical black dashed line. (D-I) APT measurements of the 3D distribution of
493 ions through a typical DSCO sample. In all images, the Cr ions are show together with one
494 other ion. (D) D ions (purple spheres). (E) D_2 ions (orange spheres). (F) H ions (yellow
495 spheres). (G) DO ions (green spheres). (H) D_2O ions (turquoise spheres). (I) OH ions (teal
496 spheres). (J) Concentration of ions in at. % measured by APT of a DCSO sample with depth
497 across the Cr capping layer (Cr, grey shaded region) Deuterium irradiated rim (DI, blue
498 shaded region) and the non-Deuterium irradiated olivine (Ol, green shaded region) deeper
499 into the mineral revealing the variation in the abundance of Cr (grey line), D (purple line), D_2
500 (orange line), DO (red line), D_2O (blue line), H (yellow line), and OH (green line) ions. Line
501 widths have been adjusted to represent the 1 sigma uncertainty and depth profiles are absolute
502 abundances not relative concentrations (**Data S1**). The boundary between the Cr and DI layer
503 is marked by a vertical dashed red line and the boundary between the DI and Ol layer is
504 marked by a vertical black dashed line.

505

506 **Fig. 3. Graph of particle diameter vs abundance of water in atomic percent (mol. %)**
507 **generated by solar wind irradiation.** A variety of extraterrestrial materials are shown, each
508 of which has a space weathered rim of different thickness: (1) Lunar soil (200 nm, dark blue
509 line); (2) IDPs and maturely space weathered Itokawa particles (100 nm, light blue line); (3)
510 the sub-mature Itokawa grain in this study (50 nm, green line); (4) a very thin space
511 weathered surface (10 nm, red line). Representative grain sizes and water abundances for
512 different extraterrestrial materials are labelled on the graph. We assume a spherical particle in

513 all cases, and as such they represent the minimum solar wind derived water contents for
514 particles of these diameters. Fractal grains will have a larger surface area and therefore a
515 greater solar wind irradiation derived water component. Particles <1 μm can entrain and store
516 several mol. % of water derived from solar wind irradiation.

517

518 **Fig. 4. Diagram of the D/H ratio that results from mixing solar wind irradiated fine**
519 **grained particles and chondritic water reservoirs.** The D/H ratio plot is generated by
520 mixing water reservoirs of carbonaceous chondrite (CR[green volume], CI [blue volume],
521 CM [orange volume], Cav [red volume, the average of CR,CI and CMs D/H =
522 0.000173[[1,16]]; water abundance = 2-16 molecular % per atom[[9]]), ordinary chondrite (
523 purple volume, OC)[19] and enstatite chondrite (brown volume, EC)[10] material, and small
524 (<100 μm) space weathered particles (D/H = 0.0000002[[26]]; water abundance = 0.1-1.6
525 molecular % per atom that can reproduce the SMOW and Bulk Silicate Earth (BSE) D/H
526 ratio[1,17] (horizontal black dashed lines **Data S3)**. The upper and lower bounds of each colored
527 field represent the upper and lower limits of the water content within the chondrites and solar
528 wind irradiated particles. The relative mass contributions that span BSE and SMOW D/H
529 ratios indicates the range of potential mixtures of theses extraterrestrial water reservoirs that
530 could generate the present-day D/H of Earth's oceans. We also plot D/H ratio produced by
531 the mixture of EC vs Cav material (pink line).

532

533 **Table 1: Summary table of the D/H ratio and water abundance in wt. % and mol. %* of**
534 **extraterrestrial and terrestrial materials.** Data from this study and [1,2,4,6,10,16,18,19,26,68-72].
535 Uncertainties are one sigma.

536

Methods

Sample preparation

Itokawa

Itokawa particle RA-QD02-0279 was mounted on the end of a glass rod with resin (**Fig. 1A-B**) in the Pb clean lab facility at the Scottish Universities Environmental Research Centre (SUERC). The mounting rod is a typical micro-computed tomography sample mount and was prepared at the Natural History Museum, London, by drilling a hole in the top of a pin and placing a 100 μm diameter glass rod inside the hole and sealing it with wax. A drop of resin was used to affix the Itokawa grain to the apex of the glass rod to provide access to the majority of the sample's surface. The sample has been stored in contact with the terrestrial atmosphere since it was received from the Japanese Aerospace Exploration Agency (JAXA) Hayabusa Curation facility on the 30th June 2017.

San Carlos olivine (SCO)

To corroborate the Itokawa atom probe tomography (APT) results a set of pristine and irradiated San Carlos olivine (SCO) reference materials were produced.

Pristine SCO

One fragment of SCO (PSCO) was mounted in resin and polished flat with a water based polishing suspension. PSCO was dried and exposed to the terrestrial atmosphere in the laboratory for several months.

Deuterium-Irradiated San Carlos Olivine (DSCO)

Preparation for Irradiation

561 Saw-cut slices of a single crystal of SCO, 2-3 mm in thickness, were hand polished to 1 μm
562 and diced into pieces approximately 2-3 mm on a side. These SCO pieces were separated into
563 two sets of six sub-samples, set A and set B. Each set was mounted polished-side-up onto a
564 25 x 25 x 1 mm thick Ta foil (99.9% purity, Goodfellow) using pieces of adhesive carbon
565 conductive tabs (Pelco, Ted Pella) cut to match the size of each sample. The high atomic
566 number metal foil and limited extent of the carbon adhesive were chosen in order to minimize
567 potential sputter cross-contamination of the polished olivine surfaces during irradiation.
568
569 *Deuterium irradiation of SCO samples (DSCO)*
570 Deuterium irradiation of all DSCO samples was performed using a 10 kV Colutron G-1 ion
571 accelerator at the Sandia National Laboratories Ion Beam Laboratory. Two irradiation
572 experiments were performed at nominally room temperature with D_2^+ ions with energies of
573 10 keV (for set A) and 2 keV (for set B). The D_2^+ ions disassociate upon contact with the
574 surface and are implanted as a charged and uncharged D isotope, each with half the energy (5
575 keV and 1 keV, respectively).
576
577 The samples for each irradiation experiment were mounted at once in the *ex situ* irradiation
578 chamber, which was pumped down to a vacuum of ~10^{-7} torr. No heating or cooling elements
579 were utilized during the experiment, and beam heating was expected to be minimal. The
580 deuterium beam was continuous and focused to about 5 mm, and each sample was irradiated
581 to a fluence of approximately 10^{19} ions/cm^2. The fluence was determined by measuring the
582 current impinging on the stage during the experiment.
583
584 *DSCO Sample Transport*

585 Adsorbed and absorbed water is not a major concern because the isotopic signature of
586 deuterium is distinguishable from that of hydrogen. Nevertheless, irradiated surfaces are
587 generally hygroscopic, and we sought to minimize uptake of ambient water vapor during
588 transporting of the samples between University of Hawai‘i at Mānoa, Sandia National
589 Laboratories, University of Glasgow and Curtin University. DSCO samples were stored
590 together with a desiccant canister (DriCan, Ted Pella) in a sealed container (Spi-Dry sample
591 preserver, SPI Supplies) back-filled with dry Ar gas prior to and following deuterium
592 irradiation. Pairs of sub-samples from sets A and B were placed in membrane boxes with a
593 hole in one side and then vacuum packed with desiccant beads for expedited shipping for
594 APT experiments.
595
596 *Helium-Irradiated San Carlos Olivine (HeSCO)*
597 Single-crystal olivine was irradiated with 4 keV He^+ under ultra-high vacuum in a specialized
598 surface science instrument (PHI 560; P= 9 x 10^{-10} Torr) at the University of Virginia,
599 described in previous publications (e.g. [73,74]). The olivine mineral was cleaved in air, prior to
600 insertion into vacuum and mounted on a copper plate. X-ray photoelectron (XPS) spectra
601 were taken prior and post irradiation at regular fluence intervals, confirming chemical
602 reduction ($Fe^{3+} \rightarrow Fe^{2+} \rightarrow Fe^0$) of iron with simultaneous preferential removal of oxygen and
603 (atmospheric) carbon atoms. Helium ions were generated in an electron-bombardment source
604 at 4 kV and rastered over 6 x 6 mm^2 for uniform irradiation, providing an average flux of 4.9
605 x 10^{13} ions cm^{-2} s^{-1} to a final fluence of 9.2 x 10^{17} He^+ cm^{-2}. A low-energy electron flood gun
606 was used during irradiation to neutralize surface charge. Samples were then removed from
607 vacuum and stored at atmosphere, before subsequent transport to NASA Johnson Space
608 Center for analytical electron microscopy and focused ion beam (FIB) sectioning followed by
609 transport to Curtin University.

610

611 **High vacuum low kV scanning electron imaging**

612 Low accelerating voltage scanning electron microscopy (SEM) surface imaging including
613 secondary electron images of Itokawa particle RA-QD02-0279 was undertaken to identify
614 mineral phases and space weathering features such as micrometeorite impact craters (**Fig.**
615 **1A-B, S1-2**) to target for subsequent analysis. A low accelerating voltage (5-15 keV) was
616 used to minimize the possibility of mobilizing volatile phases and devolatilizing the space
617 weathered surfaces of these particles. SEM characterization of particle RA-QD02-0279 was
618 undertaken on the Tescan Mira3, variable pressure field emission gun (VP-FEG)-SEM at the
619 John De Laeter Centre, Curtin University.

620

621 **Focused ion beam (FIB)-SEM sample preparation for transmission electron microscopy**
622 **(TEM) and APT**

623 All samples were coated with 200 nm of Cr using a Cressington 208HR sputter coater at the
624 John de Laeter Centre, Curtin University. Coating thickness was determined using a crystal
625 thickness monitor and the 200 nm Cr coating was achieved by depositing eight 25 nm layers
626 with a 2-minute pause between layers to minimize sample heating. The Cr coating was
627 applied in order to protect the samples during focused ion beam (FIB)-SEM sample
628 preparation for APT and transmission electron microscopy (TEM), as well as to function as a
629 fiducial marker for the location of the grain surface in FIB-SEM preparation and within the
630 APT datasets. Cr was chosen due to the low concentration of Cr in olivine and because it has
631 a similar ionization potential to silicate phases. Therefore, during APT analysis the voltage
632 and laser energy required to achieve stable field evaporation between these two materials will
633 be similar and will minimize the risk of analysis artefacts and failure.

Several specimens of each sample (Itokawa RA-QD02-0279: front [5, **Fig. 1A and S1**] and back [5; **Fig. 1B, S2**]; PSCO [5]; and DSCO [5], were prepared for APT using the Tescan Lyra3 dual beam FIB-SEM at the John De Laeter Centre, Curtin University following the typical lift out method described in detail in Thompson et al., [75]. Additionally, one 5×10×0.1 µm TEM sample was extracted from Itokawa particle RA-QD02-0279 using the Tescan Lyra3 dual beam FIB-SEM at the John De Laeter Centre, Curtin University. This FIB-SEM uses a mono-isotopic liquid metal ion source of $^{69}Ga^{+}$ as a high precision milling beam. In brief, APT specimens were prepared from the region of interest in each sample by depositing a protective layer (2.5×10 µm) of Pt, firstly by electron beam deposition (200 nm thick) and then by ion beam deposition (1 µm). This layer was then undercut using the FIB to produce a wedge 15 µm in length. One end was cut free and attached to a micromanipulator with a Pt weld. The specimen was then cut free from the main mass of the sample and extracted. Prism shaped segments with 2.5 µm top edges of the wedge were placed, point down, so as the space grain surface of the sample was facing up, onto a pre-grown silica post on a microtip coupon with a Pt deposition and cut free. This process was repeated until all the wedge had been placed on posts. The samples were then shaped using a progressively smaller annular milling pattern and lower beam current in order to produce a fine <100 nm tip diameter needle specimen. Care was taken to ensure all the Pt was milled away but a small amount (~50 – 100 nm) of Cr remained at the tip of the needle to ensure the preservation of original surface (**Fig. S1C-H, 2D-H**). A final milling process at 2 kV accelerating voltage was performed to remove the top ~20 nm of damaged material produced by the high energy Ga^{+} ion implantation.

TEM methods

The electron transparent lamella was used for transmission electron microscopy (TEM) analysis on a FEI Talos FS200X G2 TEM/scanning TEM (STEM) microscope operated at 200 kV and equipped with a Super-X energy dispersive X-ray spectrometer (EDS) system located in the John de Laeter Centre in Curtin University. Bright Field (BF) imaging was used for high magnification imaging. STEM images and EDS data were captured with a beam current of 0.6 nA. STEM imaging included BF, Dark Field (DF) and High Angle Angular Dark Field (HAADF) imaging modes. EDS data was collected using FEI Velox software version 2.4.

Atom probe tomography

All APT specimens were analysed on the Cameca Local Electrode Atom Probe (LEAP) 4000X HR Geoscience atom probe, housed at the John de Laeter Centre, Curtin University. The analytical conditions for each run can be found in **Fig. S8**. All analyses were performed in laser assisted mode using an ultraviolet laser (λ = 355 nm). Four samples from Itokawa particle RA-QD02-0279 (two front **Fig. S1E, G**, [Itokawa1 and Itokawa2] and two back **Fig. S2F, H** [Itokawa4 and Itokawa3]), one sample from PSCO and three samples from DSCO ran successfully in the APT (**Fig. 2, S3-4)**. These APT samples all initially began field evaporation in the Cr capping layer before passing through any rim feature and into the main material.

The bulk composition of each APT specimen was calculated by measuring the full width half maximum of peaks in the mass to charge spectrum (**Fig. S5**). The same range file was used for all APT samples with additional peaks attributed to the DSCO datasets for D, D_2, DO and D_2O. The counting statistical uncertainty for each measured ion peak within the APT datasets was established through the formula below from [76].

$$s = \sqrt{A + B}$$

683 Where s is the counting statistical uncertainty, A is the total counts beneath a ranged peak
684 including background and B is the average background counts over the same range. These
685 uncertainties were propagated throughout. In all cases the uncertainties calculated in this way
686 were low (<5 %) and had negligible impact on the implications of the study.
687 Additional sources of uncertainty in APT data that should be considered are derived from
688 detector dead times[77-79]. However, this is only a significant consideration when reporting
689 isotope abundances for light elements. As such it is not accounted for in the present study
690 which only reports major element and molecular abundances.
691 Features present in the sample surface such as chemical profiles were identified in APT
692 datasets by producing a depth profile using a cylindrical region of interest across the Cr cap
693 and the sample material summing the elemental molecular concentrations over 2 nm bin sizes
694 (**Data S1**). Additionally, density fluctuations in the surface of the material were identified
695 through generating isosurfaces related to the density of ions collected for each element.
696
697 <u>The bulk olivine</u>
698 In all Itokawa APT olivine samples, $^{1}H^{+}$ (~1 u/Q; u = unified atomic mass unit, 1 u is 1/12 of
699 the mass of ^{12}C and Q = the charge in Coulombs) steadily increases with depth within the
700 olivine (**Fig. 2A-C, S3**). This signal is generated by adsorption of residual H on the specimen
701 surface in the UHV chamber and should be considered as noise. This background H level is
702 dependent on a number of factors such as tip shape, the material that is field evaporating, the
703 field around the needle, the temperature and humidity and so can vary between analysis of the
704 same material[80]. The increase of $^{1}H^{+}$ with analysis depth (**Fig. 2, S3, S4**) is commonly
705 observed in APT datasets and is due to the increasing field around the sample generating
706 more H evaporation from the chamber as the radius of the specimen and the voltage increase
707 during analysis. In addition to $^{1}H^{+}$ we also observe other water group ions within the mass

spectrum such as $^{16}O^{1}H^{+}$ (17 u/Q) $^{16}O^{1}H_2^{+}$ (18 u/Q) $^{16}O^{1}H_3^{+}$ (19 u/Q) (**Fig. 2, S3-5**) and these peaks are used for the quantification of the total water content within the APT datasets. This steady enrichment of H is also observed for $^{16}O^{1}H^{+}$ (17 u/Q) (**Fig. 2, S3-5**) as some of the H within the UHV forms a complex molecular ion with O to produce OH, this trend is also typical for O bearing APT datasets. The mass peak at 17 u/Q is predominantly comprised of OH. ^{17}O is only 0.04% of the total oxygen[28] and so the contribution of ^{17}O will be below background levels as such we assume the entire 17 u/Q peak is comprised of OH ions. All other ranged ions within the samples remain at a constant level throughout the olivine component of the datasets. As will be discussed later there is a distinct drop in the abundance of H and hydroxyl ions in all Itokawa APT data sets between 40-180 nm (**Fig. S3)** from the olivine grain surface. This drop cannot be generated by a change in the field and is a real property of the H content of the mineral.

The total abundance of H and OH is not constant between APT analysis of the same material as such each sample must be corrected separately. The mass peak at 18 u/Q is a result of the combination of ^{18}O and H_2O ions, ^{18}O is 0.2% of the total oxygen[28] so will have some contribution to the 18 u/Q peak in addition some of the H_2O ions will be derived from the combination of ^{16}O with H_2 from the UHV chamber. The mass peak at 18 u/Q was deconvolved to extract the $^{1}H_2{}^{16}O^{+}$ contribution from the $^{18}O^{+}$ signal assuming a solar $^{16}O/^{18}O$ ratio[28](*9*) to determine the total contribution form H_2O ions to the 18 u/Q peak. To calculate the average and maximum total content over the Itokawa samples and the deuterated water content of the DSCO samples, all relevant H (H, H_2, H_3, H_4, OH, H_2O H_3O) species or D (D, D_2, OD, D_2O) species respectively were ranged using the full width of the peak. To determine the total water component of the bulk olivine, atomic % (at. %; number of atoms per 100 atoms) totals for each species were calculated by determining the proportion of atoms relative to the total number of atoms under ranged peaks in each dataset extracted

733 from a volume of interest within the bulk olivine material away from any irradiated surface or
734 Cr interface (typically the volume defined by the final 20 nm of the analysis). The sum of the
735 measured at. % of all relevant H species were added together to produce molecular % (mol.
736 %) totals for water, where mol. % is the number of molecules of water per 100 atoms. From
737 these calculations we can determine that Itokawa olivine APT datasets comprise ~0.5 ± 0.05
738 mol. % water, DSCO comprise ~0.5 ± 0.05 mol. % water, and PSCO comprise ~0.6 ± 0.05
739 mol. % water. The water abundance in the bulk olivine of Itokawa DSCO and PSCO is
740 substantially higher than the 100-300 parts per million by weight water content measured
741 from bulk olivine in Itokawa grains, LL chondrites and terrestrial olivine[45,51]. This indicates
742 that the majority of the calculated bulk olivine water content in these APT data sets are
743 derived from surface reactions with H_2 in the UHV. This represents a normal UHV
744 contribution of water to the total abundance in each APT sample and allows us to detect
745 deviations from this normal level within the rest of the dataset. To do this, a cylindrical
746 region of interest was generated through each APT data to produce an at. % concentration
747 depth profile (**Fig. 2, S3, S4, S6, Data S1**) This is an absolute concentration and not a relative
748 abundance as such variations in minor species are not a result of heterogeneity in major
749 species. The data was averaged over 2 nm thick segments. The average background H (mol.
750 %) sum of all H or D species was generated from a summed average of all relevant species
751 from the basal 10 nm of the sample well within the olivine and away from the irradiated
752 surfaces as a proxy for the typical APT background. It should be noted that even D species
753 have a nominal background from isobaric interferences with H species. This background
754 water level was subtracted from the water content of each 2 nm segment to generate a real
755 water signal. The average water content was then calculated from the irradiated rims.
756
757 Irradiated surfaces

There is no variation within the PSCO for any ion species approaching the olivine grain surface (**Fig. S4V-X**). In particular, the H remains constant within the PSCO olivine grain surface (**Fig. S4V-X**). Within the DSCO and Itokawa APT data sets, the H abundance diminishes slightly within the space weathered or artificially irradiated rim (**Fig. 2, S3, S4A-N**). This depletion of H ions is more pronounced within the DSCO. In addition, OH (17 u/Q) is also depleted within the DSCO surface (**Fig. 2D-J, S4A-N**). This enhanced depletion of H in the DSCO is likely caused by the presence of D and corresponding absence of H. Within the DSCO, there is a pronounced 2-3 mol % enrichment in D (2 u/Q), D_2 (4 u/Q) DO (18 u/Q) and D_2O (20 u/Q) in the outermost 40 nm of the grain (**Fig. S4A-N, S5D**). In the Itokawa sample, APT data enrichments in H_2O and OH are observed in the upper 40-60 nm of the sample (**Fig. S3, S5A-C**). To calculate the total average water content in the space weathered rim, the sum of the 17, 18 and 19 u/Q peaks representing $^{17}O^{+}+{}^{1}H^{16}O^{+}$, $^{18}O^{+}+{}^{1}H_2{}^{16}O^{+}+{}^{1}H^{17}O^{+}$ and $^{1}H_3{}^{16}O^{+}+{}^{1}H_2{}^{17}O^{+}+{}^{1}H^{18}O^{+}$ respectively was averaged over the depth of the enrichment, while the total maximum water enrichment was measured from the maximum value detected within the rim. The average water content calculated previously from the bulk olivine was then subtracted from this value to give the total average water, and total maximum water derived from solar wind irradiation. Revealing a maximum of 1.6 mol. % (**Fig. S1E**), 1.4 mol. % (**Fig. S1G**), 0.24 mol. % (**Fig. S2F**), 0.7 mol. % (**Fig. S2H**) total enrichment in water species and an average of 0.8 mol. % (**Fig. S1E**), 0.7 mol. % (**Fig. S1G**), 0.16 mol. % (**Fig. S2F**), 0.47 mol. % (**Fig. S2H**) total enrichment in water species in the upper 50 nm (**Fig. S1E**), 60 nm (**Fig. S1G**), 180 nm (**Fig. S2F**), and 30 nm (**Fig. S2H**) of the grain (**Fig. S3**).

Sputter coated Cr layer

782 The H peak decreases substantially in the Cr cap within the DSCO and Itokawa samples but
783 increases within the PSCO APT dataset (**Fig. 2, S3, S4**). In the Itokawa and DSCO datasets
784 where more of the Cr cap is preserved H fluctuates within the cap (**Fig. S3, S4A-N**). This is
785 likely caused by porosity within the sputter coated capping layer subtly changing the
786 ionization environment. As such, in all APT datasets the majority of this H signal in the Cr
787 layer is likely to be derived from reactions between H from the UHV system and the Cr layer.
788 In the PSCO the increase in H in APT data is mirrored by a complementary increase in OH^+
789 and H_2O^+ ions suggesting at least some contribution to these mass peaks is from reactions
790 between H from the UHV system and the Cr layer (**Fig. S4**). In addition, the sputter coated Cr
791 layer is impure and contains a substantial proportion of O in the form of $CrO^{+ \text{ and } ++}$ ions (**Fig.**
792 **S5A**), as such some of the enrichment in OH^+ and H_2O^+ in the Cr layer is derived from $^{17}O^+$
793 and $^{18}O^+$ isobaric interferences. This also explains the trend in OH and H_2O abundances in
794 the DSCO and Itokawa APT datasets where OH and H_2O decrease in the Cr layer and then
795 plateau at a lower level than the olivine (**Fig. 2, S3, S4A-N**), revealing the presence of
796 residual O in the Cr layer. Cr metal reacts rapidly when exposed to the terrestrial atmosphere
797 to form CrO and as such the presence of O within the sputter coated Cr layer is expected. In
798 two DSCO samples (DSCO1 and DSCO3) **(Fig. 2D-J, S4A-G and 4O-U)** the Cr cap has a
799 lower concentration of Cr relative to DSCO2, PSCO and Itokawa. This is because these two
800 DSCO samples had a substantially thinner Cr layer remaining after FIB preparation meaning
801 the APT analysis only briefly measured the Cr layer prior to transitioning to the DSCO
802 olivine, consequently producing a lower Cr concentration in the Cr capping layer. In the
803 DSCO there is some residual signal from D^+, and D^{2+}, DO^+ D_2O^+ present in the Cr layer, this
804 is due to isobaric interferences with, H_2^+, H_4^+, and $^{18}O^+$ and $^{40}Ca^{++}$ within the sputter coated
805 Cr capping layer and is observed in all APT samples.
806

The effect of the Cr-olivine contact

Cr is enriched within the sputter coated Cr layer as expected. However, in several cases the olivine grain surface is irregular and not normal to the Z-direction of the APT analysis. Thus, the depth profile generated by the wide cylindrical regions of interest in the z-direction of each APT analysis mean the onset of Cr enrichment and hydrous depletions in the DSCO and Itokawa APT data do not perfectly correlate due to the morphology of the grain surface with respect to the region of interest (**Fig. 2, S3, S4, S6**). Extracting a thinner cylinder for our region of interest depth profile reveals that the Cr enrichment and hydrous ion depletions are correlated and relate to the compositional change between the sputter coated Cr and olivine grain surfaces (**Fig. S6**). However, demonstrating this correlation comes at the cost of the counting statistical uncertainty and as such the variations in hydroxide species are less clear (**Fig. S6**). Thus, we chose a cylindrical diameter that acted as a compromise between increasing the amount of data included while preserving the boundary.

In some APT datasets Itokawa 1, Itokawa 2, and DSCO3, there is a minor enrichment trend in H OH and H_2O at the boundary between Olivine and Cr (**Fig. 2, S3, S4)**. This minor enrichment is consistent with variable H and H2O contamination on mineral surfaces sometimes observed and can affect APT datasets to varying degrees[80]. This boundary enrichment in H species is distinct from the secondary enrichment in H species that is 40 nm beneath the surface of the olivine in Itokawa APT data and in deuterium species in DSCO samples (**Fig. 2, S3, S4)** which we interpret as real H or D respectively implanted by the solar wind or irradiation experiments respectively.

Grain size dependence on solar wind derived water abundance.

The contribution of the solar wind derived water to the total water budget of an olivine grain was modelled varying the space weathering rim thickness between 10 nm and 200 nm, which

832 are typical widths of space weathering surfaces[30,45,50] and varying the grain size between 0-
833 1×10^9 nm. We assume the grain is spherical for simplicity, but it should be noted that the
834 resulting water abundance values will be the minimum value of a particle of that size. We
835 calculated the percentage of the volume of each grain that is affected by space weathering
836 and use the APT data to define the minimum water content present within the space
837 weathered volume to be 1.6 mol. %. We then calculated the total water content for the whole
838 grain (**Data S2**). These were then compared to typical grain sizes for a variety of known
839 extraterrestrial materials to generate **Fig. 3**.
840
841 **Earth ocean contribution model**
842 The range of possible water contributions from known Solar System water reservoirs to
843 reconcile Earth's oceans was modelled to work out the possible contributions of water from
844 water-rich chondritic asteroids, and solar wind sources that could reproduce Earth's ocean
845 D/H ratio. We assume the contribution of meteorite sized objects to be negligible given the
846 bimodal size distribution of objects falling to the Earth[55-58]. We included bulk anyhydrous
847 ordinary chondrites and enstatite chondrites in our model despite the fact that their overall
848 contribution is likely to be small due to their low water content[10,19,81] which is only
849 compatible with the lowest estimate for the water content of the bulk Earth (**Table 1**), as such
850 we focus on the aqueously altered water-rich CM, CI and CR chondrites[1,16,71,81]. We assumed
851 a D/H ratio of 1.73×10^{-4} [1,4] and water abundance of 2-16 mol. %[71,81] from water rich
852 carbonaceous chondrites (an average of CM (D/H 1.48×10^{-4} [1,16]), CR (D/H 2.57×10^{-4} [1])
853 and CI (1.68×10^{-4} [1]) based on their current relative abundance in the meteorite collection
854 [CR: 22.3 % CM: 76.6 % and CI: 1.1% [82]], an average D/H ratio of 1.31×10^{-4} [1,4] and
855 water abundance of 0.1-0.8 mol. % for enstatite chondrites, an average D/H ratio of 1.35×10^{-4}
856 [10] and water abundance of 0.1-0.7 mol. % for ordinary chondrites[19] and a D/H ratio of $2\times10^{-}$

[7] [4,26] and water abundance of 0.1-1.6 mol. % for solar wind derived water in small particles. The mol. % abundance of water rich chondrites, ordinary chondrites enstatite chondrites and Earth was converted from the wt. % of water in each object (Table 1; 1.6-12.9 %, 0.8-0.54 % and 0.02 % respectively) using the equation below

$$Water_{(Mol.\%)} = \frac{\left(\frac{Water_{(wt.\%)} \times A_N}{Mr_{(H_2O)}}\right) \times 100}{\left[\left(\frac{Water_{(wt.\%)} \times A_N}{Mr_{(H_2O)}}\right) + \left(\frac{(100 - Water_{(wt.\%)}) \times A_N}{Mr_{(bulk)}}\right)\right]}$$

Where A_N is Avogadro's constant (6.022×10^{23}), $Mr_{(H2O)}$ is the molecular mass of water (18 g/mole), $Mr_{(bulk)}$ is the average molecular mass of the body in question sans water (21.2 g/mole for the Bulk Silicate Earth[69], 24 g/mole for carbonaceous chondrites[70], 25.6 g/mol for enstatite chondrites and 24.4 g/mol was used for ordinary chondrites[70]). We modelled the mixture of each of these reservoirs, and our newly defined water budget of space weathered fine-grained particles. By allowing the mass proportion of each reservoir to vary we calculated solutions for this two-component model for each Solar System water source using the equation below.

$$D/H_{(average)} = \left[\frac{\left(Mass\ fraction_{SW} \times SW_{water\ (Mol.\%)} \times D/H_{SW}\right) + \left((1 - Mass\ fraction_{SW}) \times Asteroid_{water_{(Mol.\%)}} \times D/H_{Asteroid}\right)}{\left(Mass\ fraction_{SW} \times SW_{water\ (Mol.\%)}\right) + \left((1 - Mass\ fraction_{SW}) \times Asteroid_{water_{(Mol.\%)}}\right)}\right]$$

This allowed us to determine mass proportions of each material relative to fine grained solar wind irradiated particles that can reproduce the present-day surface mean ocean water (SMOW) D/H ratio of 1.557×10^{-4} and the Bulk Earth D/H of 1.49×10^{-4} of the Earth[1,17] (**Data S3**).

Our model is consistent for the assumptions outlined above however, it should be noted that a recent study from Vacher et al., [83] showed that water rich chondrites may have adsorbed substantial amounts of water from the terrestrial atmosphere. This would serve to increase, on

876 average the D/H ratio of water rich chondrites[83] which would in turn increase the contribution
877 of fine-grained solar wind irradiated particulates required. In addition, the total mol. % water
878 of water rich chondrites would be lower once terrestrial adsorbed water was removed[83] which
879 would serve to reduce the contribution of fine-grained solar wind irradiated particles
880 required. However, the amended water abundance values of Vacher et al., [83] are within the
881 range of our current model.

882 In addition, if we only consider the contribution of <10 μm fine grained solar wind irradiated
883 particles that would be sufficiently water-rich (Fig. 3) and that represent 1-10% by mass of
884 the total amount of fine grained extraterrestrial material incident on the Earth today[58]. This
885 would require a larger total contribution of fine-grained materials of up to 90-94 % of the
886 final 0.5 ± 0.25% of Earth's mass during the late veneer (**Fig. S7**). While this greater
887 contribution by mass of fine grained particles is consistent with the contribution of fine
888 grained particles to the mass flux of extraterrestrial materials incident on the Earth throughout
889 its history[38] it is unlikely to be the case that the debris disk was sufficiently dust rich.
890 However, if the particle size distribution of fine-grained materials during the late veneer was
891 more fine grained from that of the present day with a greater proportion by mass of <10 μm
892 particles this would serve to reduce the required fine grained contribution. An increased
893 abundance of fine grained <10 μm grains in the inner solar system is consistent with
894 numerical simulations of IDP grain size variation and distribution that predicts a high
895 proportion of ~5 μm particles in the inner solar system region[42]. In addition, the coarser
896 component of dust particles >10 μm typically comprised of fine-grained porous aggregates
897 e.g. IDPs and fragments of chondritic matrix would contain substantially more solar wind
898 derived water than predicted by our spherical grain model (**Fig. 3**) and would be comparable
899 in water content to the <10 μm grains. This would also serve to reduce the contribution by
900 mass of fine-grained dust during the late veneer.

The contribution of solar wind derived water may not only be limited to delivery from fine grained dust as during the debris disk stage all materials will experience a radiation rich environment. Thus, all dust produced during this period will incorporate solar wind derived water. Much of this irradiated material will reaccrete onto and/or form primitive asteroids. Consequently, solar wind derived water will become incorporated into the regolith of primitive asteroids as this dust is reaccreted, while many primitive asteroids likely formed from the re-accretion of fine-grained space weathered materials. Therefore, both water rich fine-grained dust and water rich asteroids/asteroid regoliths derived from the (re)accretion of this water rich dust will be produced in the early Solar System. This is consistent with evidence of space weathering and solar wind irradiation of, and incorporation into, chondritic regolith breccias[65,66] and the prevalence of rubble pile asteroids[67].

Data availability statement: The Itokawa particles are on loan to L.D. from JAXA as part of the 5th Announcement of Opportunity. They are currently stored at the University of Glasgow and any remaining fragments and samples will be returned to JAXA on the completion of the project. Because of the nature of APT measurements all atom probe samples detailed in this study have been destroyed. The SCO reference materials produced for this study are stored at Curtin University (PSCO), University of Hawaii (DSCO), and JSC (HeSCO). All data generated or analysed during this study are included in this published article (and its supplementary information files).

Methods references

1 Alexander, C. M. O. D. The origin of inner Solar System water. *Phil Trans Royal Soc* **375**, 20150384 (2017).

924 2 Marty, B. The origins and concentrations of water, carbon, nitrogen and noble gases
925 on Earth. *Earth & Planet Sci Lett* **313**, 56-66 (2012).
926 4 Robert, F. The origin of water on Earth. *Sci* **293**, 1056-1058 (2001).
927 6 Hallis, L. J. *et al.* Evidence for primordial water in Earth's deep mantle. *Sci* **350**, 795-
928 797 (2015).
929 9 Morbidelli, A. *et al.* Source regions and timescales for the delivery of water to the
930 Earth. *Met & Planet Sci* **35**, 1309-1320 (2000).
931 10 Piani, L. *et al.* Earth's water may have been inherited from material similar to
932 enstatite chondrite meteorites. *Sci* **369**, 1110-1113 (2020).
933 16 McCubbin, F. M. & Barnes, J. J. Origin and abundances of H2O in the terrestrial
934 planets, Moon, and asteroids. *Earth & Planet Sci Lett* **526**, 115771 (2019).
935 17 Lécuyer, C., Gillet, P. & Robert, F. The hydrogen isotope composition of seawater
936 and the global water cycle. *Chem Geol* **145**, 249-261 (1998).
937 18 Marty, B. *et al.* Origins of volatile elements (H, C, N, noble gases) on Earth and Mars
938 in light of recent results from the ROSETTA cometary mission. *Earth & Planet Sci*
939 *Lett* **441**, 91-102 (2016).
940 19 Jin, Z. & Bose, M. New clues to ancient water on Itokawa. *Sci Adv* **5**, eaav8106
941 (2019).
942 26 Huss, G., Nagashima, K., Burnett, D., Jurewicz, A. & Olinger, C. A new upper limit
943 on the D/H ratio in the solar wind. *LPI*, 1709 (2012).
944 28 Lodders, K. Solar system abundances and condensation temperatures of the elements.
945 *Astrophys J* **591**, 1220 (2003).
946 30 Bradley, J. P. *et al.* Detection of solar wind-produced water in irradiated rims on
947 silicate minerals. *Proc Natl Acad Sci* **111**, 1732-1735 (2014).

948 38 Pasek, M. & Lauretta, D. Extraterrestrial flux of potentially prebiotic C, N, and P to
949 the early Earth. *Orig Life Evol Bios* **38**, 5-21 (2008).
950 42 Poppe, A. R. An improved model for interplanetary dust fluxes in the outer Solar
951 System. *Icarus* **264**, 369-386 (2016).
952 45 Noguchi, T. *et al.* Incipient space weathering observed on the surface of Itokawa dust
953 particles. *Sci* **333**, 1121-1125 (2011).
954 50 Keller, L. P. & McKay, D. S. The nature and origin of rims on lunar soil grains.
955 *Geochim et Cosmochim Act* **61**, 2331-2341 (1997).
956 51 Demouchy, S., Jacobsen, S. D., Gaillard, F. & Stern, C. R. Rapid magma ascent
957 recorded by water diffusion profiles in mantle olivine. *Geol* **34**, 429-432 (2006).
958 55 Zolensky, M. E. *et al.* Mineralogy and petrology of comet 81P/Wild 2 nucleus
959 samples. *Sci* **314**, 1735-1739 (2006).
960 56 Love, S. & Brownlee, D. A direct measurement of the terrestrial mass accretion rate
961 of cosmic dust. *Sci* **262**, 550-553 (1993).
962 57 Anders, E. Pre-biotic organic matter from comets and asteroids. *Nat* **342**, 255-257
963 (1989).
964 58 Flynn, G., Keller, L., Jacobsen, C. & Wirick, S. An assessment of the amount and
965 types of organic matter contributed to the Earth by interplanetary dust. *Adv Space Res*
966 **33**, 57-66 (2004).
967 65 Suess, H., Wänke, H. & Wlotzka, F. On the origin of gas-rich meteorites. *Geochim et*
968 *Cosmochim Act* **28**, 595-607 (1964).
969 66 Krietsch, D. *et al.* Noble gases in CM carbonaceous chondrites: Effect of parent body
970 aqueous and thermal alteration and cosmic ray exposure ages. *Geochim et Cosmochim*
971 *Act* (2021).

67 Walsh, K. J. Rubble pile asteroids. *Annual Review of Astronomy and Astrophysics* **56**, 593-624 (2018).

68 Greenberg, J. M. Making a comet nucleus. *Astron & Astrophys* **330**, 375-380 (1998).

69 Szurgot, M. in *Lunar and Planetary Science Conference.* 1536.

70 Anderson, D. L. & Kovach, R. L. The composition of the terrestrial planets. *Earth & Planet Sci Lett* **3**, 19-24 (1967).

71 Garenne, A. *et al.* The abundance and stability of "water" in type 1 and 2 carbonaceous chondrites (CI, CM and CR). *Geochim et Cosmochim Act* **137**, 93-112 (2014).

72 Peslier, A. H., Schönbächler, M., Busemann, H. & Karato, S.-I. Water in the Earth's interior: distribution and origin. *Space Sci Rev* **212**, 743-810 (2017).

73 Dukes, C., Baragiola, R. & McFadden, L. Surface modification of olivine by H+ and He+ bombardment. *J Geophys Res: Planet* **104**, 1865-1872 (1999).

74 Loeffler, M., Dukes, C. & Baragiola, R. Irradiation of olivine by 4 keV He+: Simulation of space weathering by the solar wind. *J Geophys Res: Planet* **114**, E3 (2009).

75 Thompson, K. *et al.* In situ site-specific specimen preparation for atom probe tomography. *Ultramic* **107**, 131-139 (2007).

76 Larson, D. J., Prosa, T., Ulfig, R. M., Geiser, B. P. & Kelly, T. F. Local electrode atom probe tomography. *New York, US: Springer Science* **2** (2013).

77 Lewis, J. B., Isheim, D., Floss, C. & Seidman, D. N. C12/C13-ratio determination in nanodiamonds by atom-probe tomography. *Ultramic* **159**, 248-254 (2015).

78 Meisenkothen, F., Steel, E. B., Prosa, T. J., Henry, K. T. & Kolli, R. P. Effects of detector dead-time on quantitative analyses involving boron and multi-hit detection events in atom probe tomography. *Ultramic* **159**, 101-111 (2015).

79 Stephan, T., Heck, P. R., Isheim, D. & Lewis, J. B. Correction of dead time effects in laser-induced desorption time-of-flight mass spectrometry: Applications in atom probe tomography. *Int J Mass Spectrom* **379**, 46-51 (2015).

80 Kolli, R. P. Controlling residual hydrogen gas in mass spectra during pulsed laser atom probe tomography. *ASCI* **3**, 1-10 (2017).

81 Alexander, C. M. D., McKeegan, K. D. & Altwegg, K. Water reservoirs in small planetary bodies: meteorites, asteroids, and comets. *Space Sci Rev* **214**, 1-47 (2018).

82 LPI. *The Meteoritical Bulletin*, 2020).

83 Vacher, L. G. *et al.* Hydrogen in chondrites: Influence of parent body alteration and atmospheric contamination on primordial components. *Geochim et Cosmochim Act* **281**, 53-66 (2020).

Competing interests: Authors declare no competing interests.

Extended D**ata:**

Extended Data Figures

Fig. S1. Back scatter electron (BSE) and in-beam secondary electron (IbSE) images of the front face of Itokawa particle RA-QD02-0279 and resulting APT specimens. A) BSE image of the front face of Itokawa particle RA-QD02-0279 after Cr coating. B) BSE image of the front face of Itokawa particle RA-QD02-0279 after Ion beam Pt deposition in preparation for sample extraction for APT. The red circles indicate where the APT lift outs were extracted from the wedge. C) IbSE (left) and BSE (right) image of needle (D) half way through annular milling. The Pt protective layer is visible as well as the Cr layer. Annular milling was continued until the Pt was removed but leaving the Cr cap. D-H) IbSE (left) and BSE images (right) of each APT needle the Cr cap is visible at the apex of each tip in the BSE images as well as the Pt weld at the base.

Fig. S2. Back scatter electron (BSE) and in-beam secondary electron (IbSE) images of the back face of Itokawa particle RA-QD02-0279 and resulting APT specimens. A) BSE image of the back face of Itokawa particle RA-QD02-0279 after Cr coating. B) BSE image of the back face of Itokawa particle RA-QD02-0279 after Ion beam Pt deposition in preparation for sample extraction for APT. The red circles indicate where the APT lift outs were extracted from the wedge. C) BSE image of the back face of Itokawa particle RA-QD02-0279 after FIB lift out. D-H) IbSE (left) and BSE images (right) of each APT needle the Cr cap is visible at the apex of each tip in the BSE images as well as the Pt weld at the base.

Fig. S3. APT data from Itoakwa. The APT needles extracted from the front face of **Itokawa particle RA_QD02_0279 shown in** Fig. **S1E (A-C) and** Fig. **S1G (D-F) and in**

from the back face shown in Fig. **S2F (G-I) and** Fig. **S2H (J-L). All data sets initially ran through Cr protective layer (grey spheres) into the olivine surface. A, D, G, and J) APT measurement of the 3D distribution of Cr (grey spheres) and OH (teal spheres) ions through a space weathered surface of this Itokawa particle. B, E, H, and K) APT measurement of the 3D distribution of Cr (grey spheres) and H_2O (blue spheres) ions through a space weathered surface of this Itokawa particle. C, F, I, and L) Concentration of ions in atomic percent (at. %) measured by APT of Itokawa** with depth across the Cr capping layer (Cr, grey shaded region) space weathered rim (SW, blue shaded region) and the non-space weathered olivine (Ol, green shaded region) deeper into the mineral revealing variations in the abundances of Cr (grey line), H (yellow line), OH (green line) and H_2O (blue line) ions**. Line widths have been adjusted to represent the 1 sigma uncertainty and depth profiles are absolute abundances not relative concentrations (**Data S1**).** The boundary between the Cr and SW layer is marked by a vertical dashed red line and the boundary between the SW and Ol layer is marked by a vertical black dashed line.

Fig. S4. APT data from DSCO (A-U) and PSCO (V-X) standards. All data sets initially ran through the Cr protective layer (grey spheres) into the olivine surface. A, H, and O) APT measurements of the 3D distribution of Cr (grey spheres) and D (purple spheres) ions through a DSCO sample. B, I, and P) APT measurements of the 3D distribution of Cr (grey spheres) and D_2 (orange spheres) ions through a DSCO sample. C, J, and Q) APT measurements of the 3D distribution of Cr (grey spheres) and H (yellow spheres) ions through a DSCO sample. D, K, and R) APT measurements of the 3D distribution of Cr (grey spheres) and DO (green spheres) ions through a DSCO sample. E, L, and S) APT measurement of the 3D distribution of Cr (grey spheres) and D_2O (turquoise spheres) ions through a DSCO sample. F, M, and T)

APT measurements of the 3D distribution of Cr (grey spheres) and OH (teal spheres) ions through a DSCO sample. G, N, and U) Concentration of ions in atomic percent (at. %) measured by APT in the DCSO sample with depth across the Cr capping layer (Cr, grey shaded region), Deuterium irradiated rim (DI, blue shaded region) and the non-Deuterium irradiated olivine (Ol, green shaded region) deeper into the mineral revealing the variation in the abundance of Cr (grey line), D (purple line), D_2 (orange line), DO (red line), D_2O (blue line), H (yellow line), and OH (green line) ions. Line widths have been adjusted to represent the 1 sigma uncertainty and depth profiles are absolute abundances not relative concentrations (**Data S1**). The boundary between the Cr and DI layer is marked by a vertical dashed red line and the boundary between the DI and Ol layer is marked by a vertical black dashed line. V) APT measurements of the 3D distribution of Cr (grey spheres) and OH (teal spheres) ions through a PSCO sample. W) APT measurements of the 3D distribution of Cr (grey spheres) and H_2O (blue spheres) ions through a PSCO sample. X) Concentration of ions measured by APT in the PSCO sample with depth across the Cr capping layer (Cr, grey shaded region), into the olivine (Ol, green shaded region). Line widths have been adjusted to represent the 1 sigma uncertainty and depth profiles are absolute abundances not relative concentrations (**Data S1**). The boundary between the Cr and Ol layer is marked by a vertical dashed red and black line.

Fig. S5. Representative APT mass spectra (left) and oxygen series peaks (right). Spectra were produced from regions of interest within: A) the sputter coated Cr layer from **Fig. S3J-L**, B) the bulk olivine of Itokawa from **Fig. S3J-L**, C) the solar wind irradiated rim of Itokawa olivine from **Fig. S3J-L**, D) D-irradiated rim from **Fig. S4H-N**.

Fig. S6. The effect that changing the diameter of the cylindrical region of interest has on the sputter coated Cr and olivine interface and on counting statistics under the peak. A) The 42 nm cylindrical region of interest used to produce the concentration profiles from the APT dataset Itokawa3 **Fig. S3J-L.** B) A 3 nm cylindrical region of interest from the APT dataset Itokawa3. C) Corresponding concentration profiles in atomic percent (at. %) for Cr and H from the 42 nm region of interest and sum Cr and H (including molecular ions) concentration profiles from the 3 nm wide cylinder. We note that the Cr-olivine interface is sharper in the 3 nm wide cylinder but it comes at the expense of the counting statistical uncertainty of the measurement. Line widths have been adjusted to represent the 1 sigma uncertainty and depth profiles are absolute abundances not relative concentrations.

Fig. S7. Diagram of the D/H ratio that results from mixing solar wind irradiated <10 μm fine grained particles and chondritic water reservoirs. The D/H ratio plot is generated by mixing water reservoirs of carbonaceous chondrite (CR[green volume], CI [blue volume], CM [orange volume], Cav [red volume, the average of CR,CI and CMs D/H = 0.000173[[1,16]]; water abundance = 2-16 molecular % per atom[[9]]), ordinary chondrite (purple volume, OC)[19] and enstatite chondrite (brown volume, EC)[10] material, and small space weathered particles, where only particles <10 μm that make up ~10 % of present day fine grained extraterrestrial dust are considered (D/H = 0.0000002[[26]] water abundance = 0.1-1.6 molecular % per atom that can reproduce the SMOW and Bulk Silicate Earth (BSE) D/H ratio[1,17] (horizontal black dashed lines, **Data S3)**. The upper and lower bounds of each field represent the upper and lower limits of the water content within the chondrites and solar wind irradiated particles. The relative mass contributions that span BSE and SMOW D/H ratios indicates the range of potential mixtures of theses extraterrestrial water reservoirs that could generate the present-day D/H of Earth's oceans.

Fig. S8. Operating conditions of the geoscience atom probe (R80). The run number for each sample and sample label are given.

Extended data references

1 Alexander, C. M. O. D. The origin of inner Solar System water. *Phil Trans Royal Soc* **375**, 20150384 (2017).

9 Morbidelli, A. *et al.* Source regions and timescales for the delivery of water to the Earth. *Met & Planet Sci* **35**, 1309-1320 (2000).

10 Piani, L. *et al.* Earth's water may have been inherited from material similar to enstatite chondrite meteorites. *Sci* **369**, 1110-1113 (2020).

16 McCubbin, F. M. & Barnes, J. J. Origin and abundances of H2O in the terrestrial planets, Moon, and asteroids. *Earth & Planet Sci Lett* **526**, 115771 (2019).

17 Lécuyer, C., Gillet, P. & Robert, F. The hydrogen isotope composition of seawater and the global water cycle. *Chem Geol* **145**, 249-261 (1998).

19 Jin, Z. & Bose, M. New clues to ancient water on Itokawa. *Sci Adv* **5**, eaav8106 (2019).

26 Huss, G., Nagashima, K., Burnett, D., Jurewicz, A. & Olinger, C. A new upper limit on the D/H ratio in the solar wind. *LPI*, 1709 (2012).

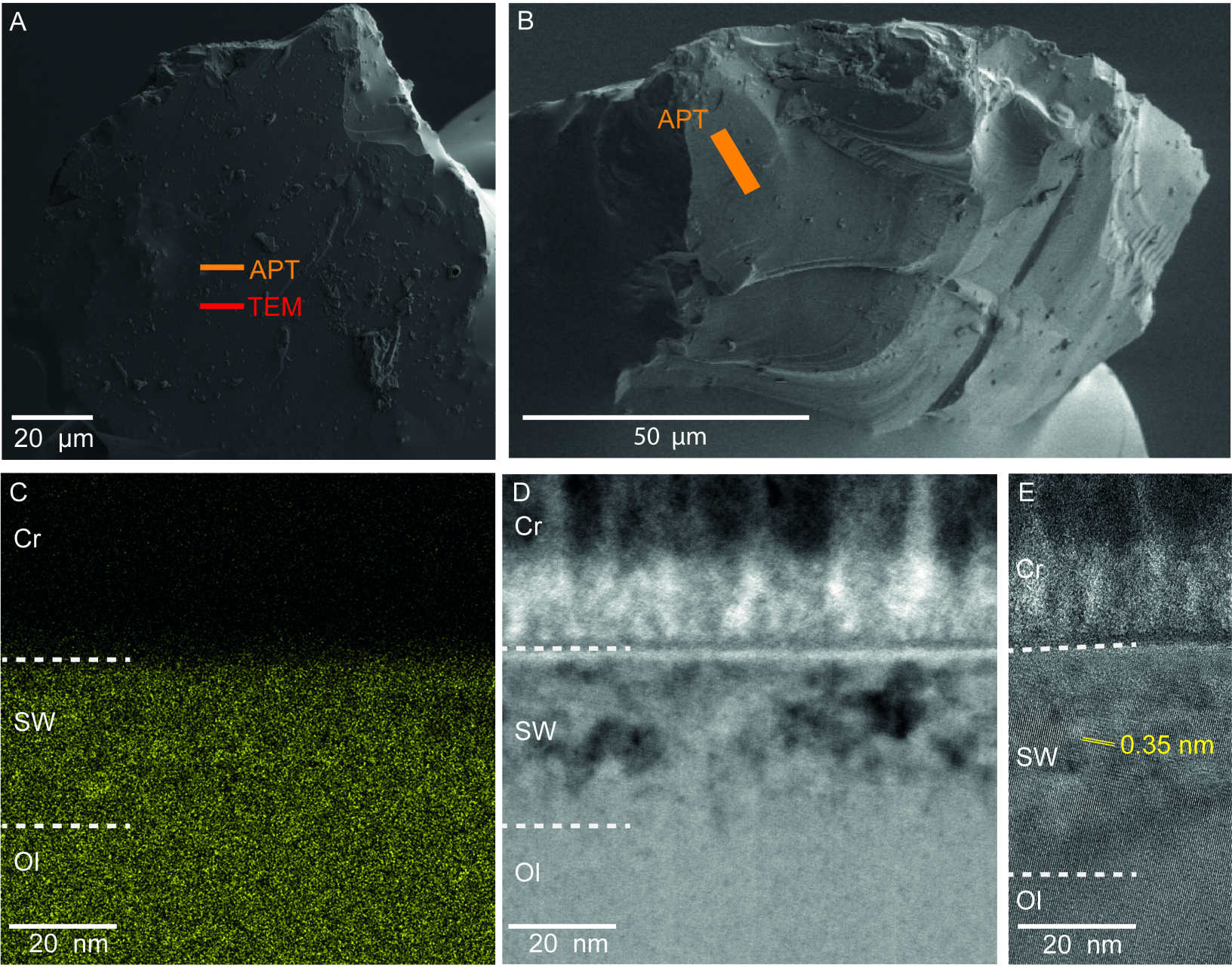
A
APT
TEM
20 µm
B
APT
50 µm
C
Cr
SW
Ol
20 nm
D
Cr
SW
Ol
20 nm
E
Cr
SW
0.35 nm
Ol
20 nm

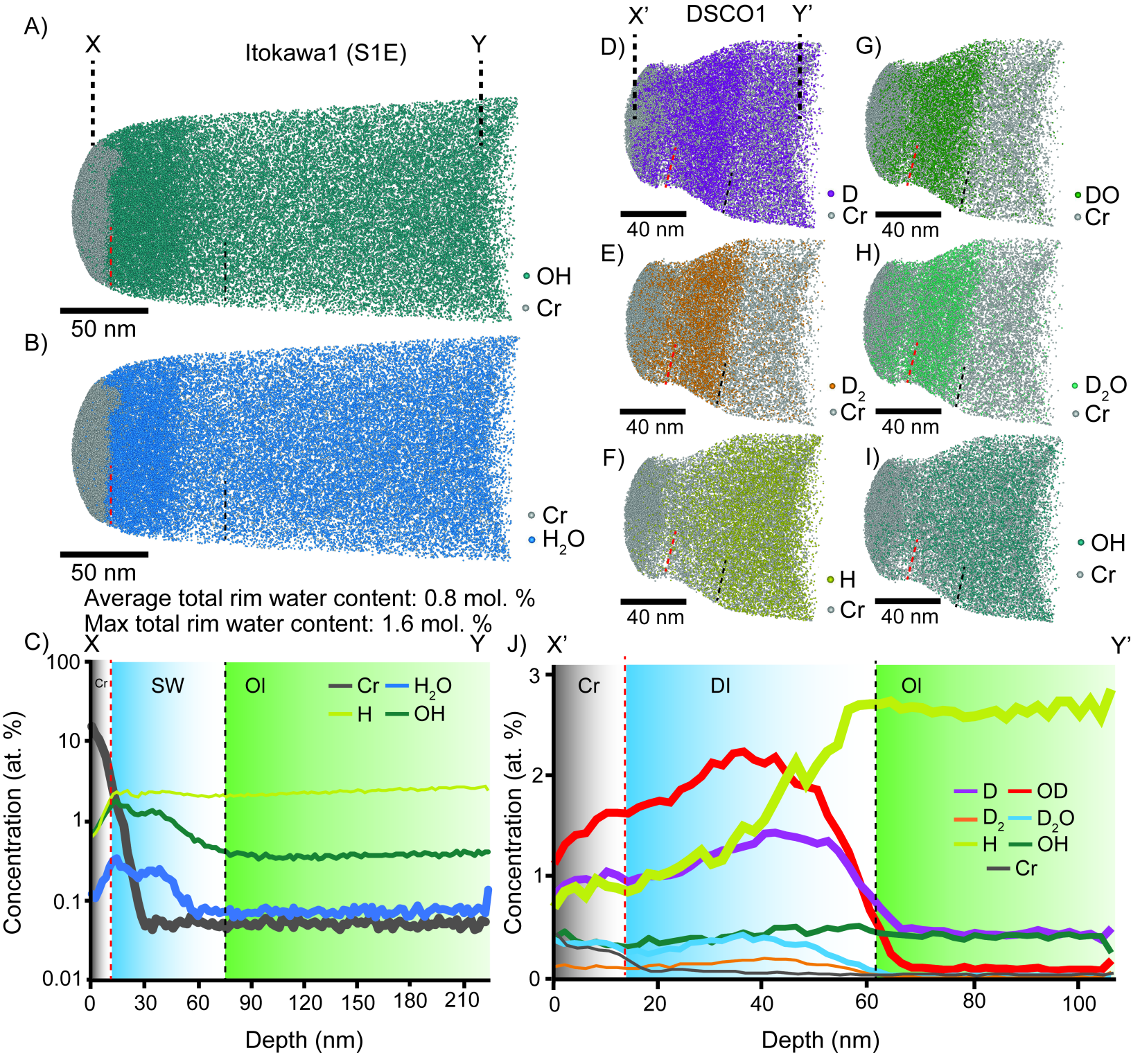
A)
X
Itokawa1 (S1E)
Y
OH
Cr
50 nm
B)
Cr
H2O
50 nm
Average total rim water content: 0.8 mol. %
Max total rim water content: 1.6 mol. %
X'
DSCO1
Y'
D)
D
Cr
40 nm
G)
DO
Cr
40 nm
E)
D2
Cr
40 nm
H)
D2O
Cr
40 nm
F)
H
Cr
40 nm
I)
OH
Cr
40 nm
C)
X
Y
Cr
SW
OI
Cr
H2O
H
OH
Concentration (at. %)
Depth (nm)
J)
X'
Y'
Cr
DI
OI
D
OD
D2
D2O
H
OH
Cr
Concentration (at. %)
Depth (nm)

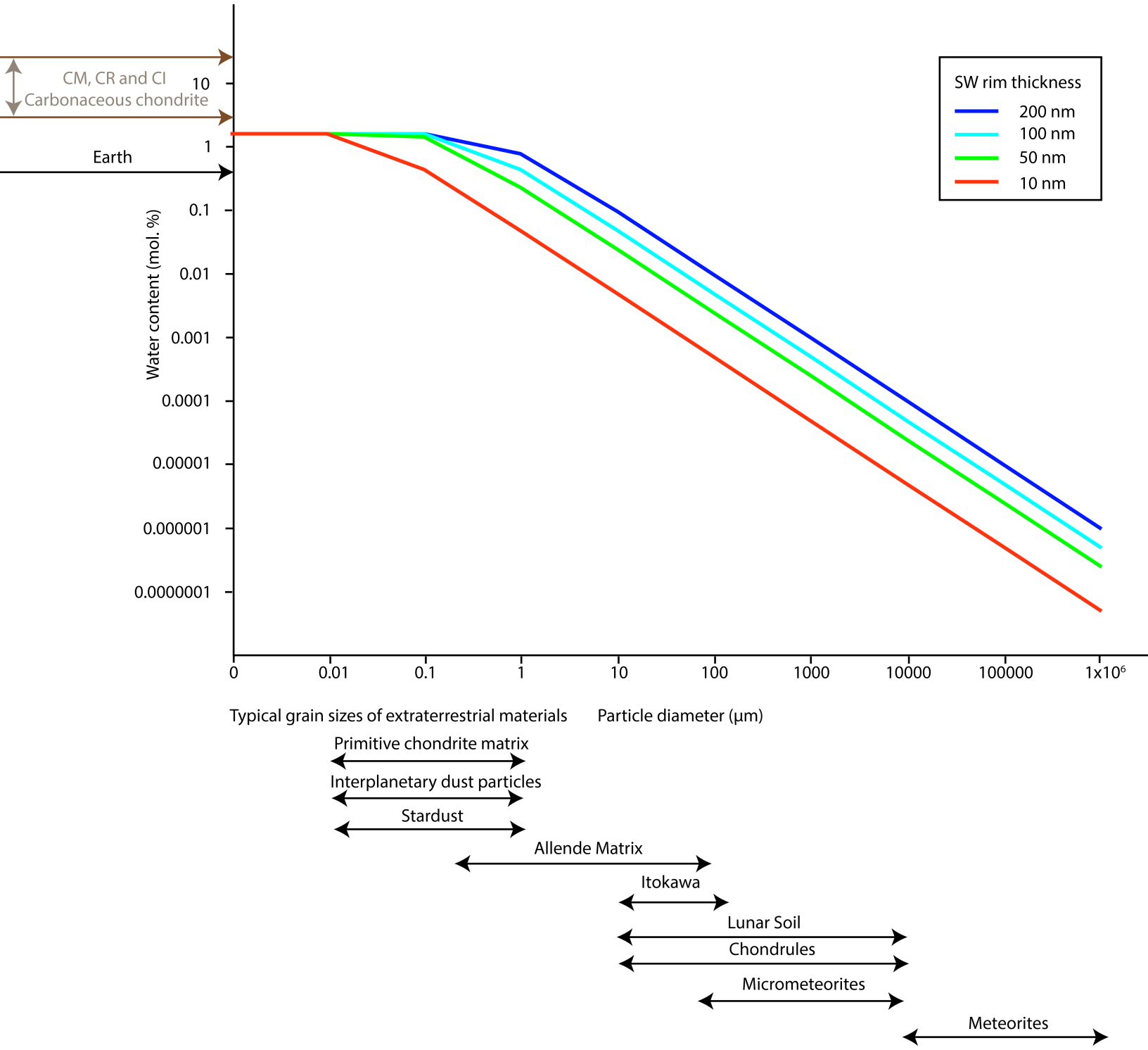
CM, CR and CI
Carbonaceous chondrite
Earth
10
1
0.1
0.01
0.001
0.0001
0.00001
0.000001
0.0000001
Water content (mol. %)
SW rim thickness
200 nm
100 nm
50 nm
10 nm
0
0.01
0.1
1
10
100
1000
10000
100000
1x10⁶
Typical grain sizes of extraterrestrial materials
Particle diameter (μm)
Primitive chondrite matrix
Interplanetary dust particles
Stardust
Allende Matrix
Itokawa
Lunar Soil
Chondrules
Micrometeorites
Meteorites

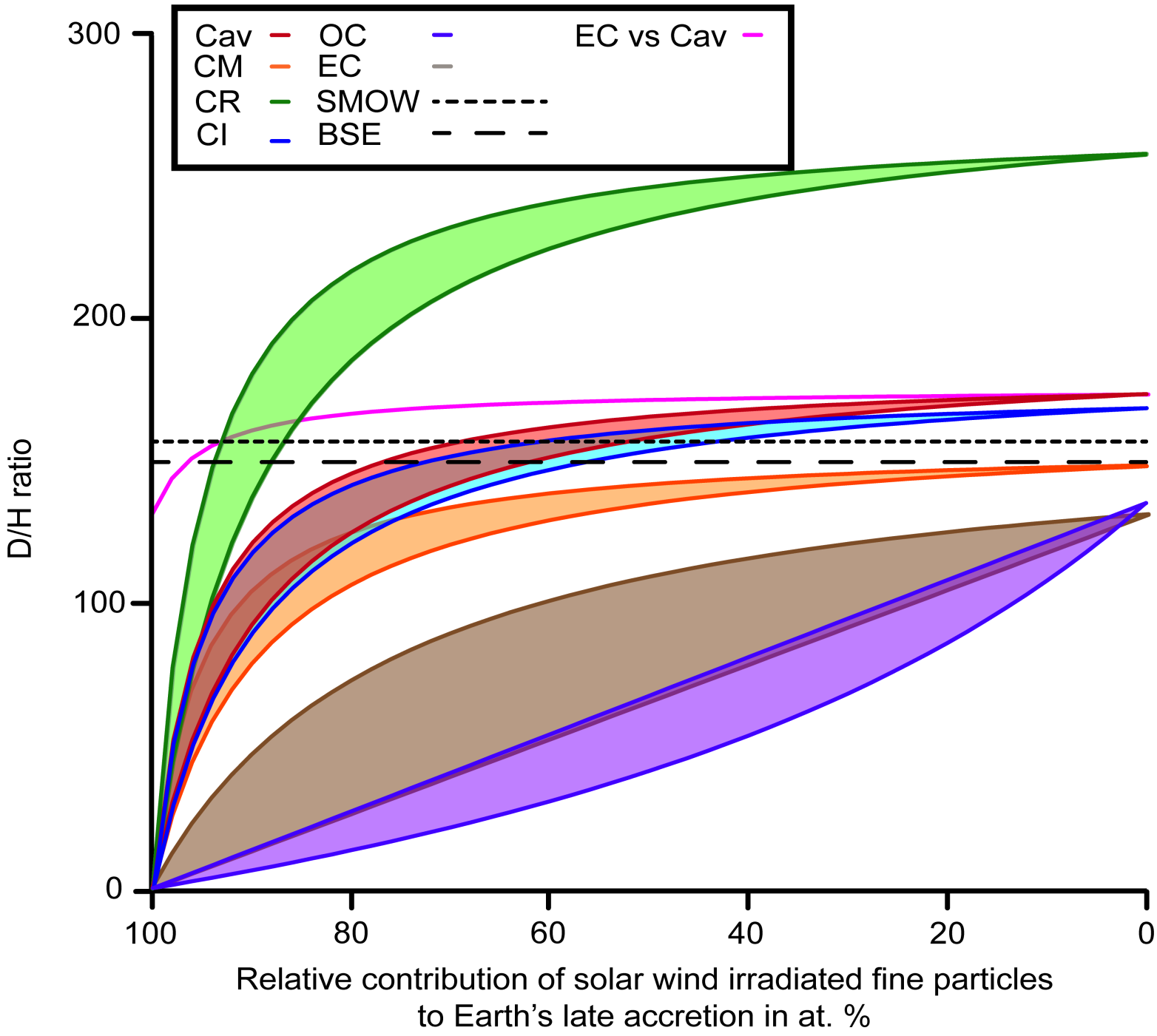
Cav
CM
CR
CI
OC
EC
SMOW
BSE
EC vs Cav
300
200
100
0
D/H ratio
100
80
60
40
20
0
Relative contribution of solar wind irradiated fine particles
to Earth's late accretion in at. %

Table 1

Extraterrestrial Water reservoirs	**wt. % water**	**Mean atomic mass**
CM meteorites	1.6-12.9	24
CI meteorites	1.6-12.9	24
CR meteorites	1.6-12.9	24
Enstatite chondrites	0.1-0.5	25.6
Itokawa/ordinary chondrites	0.1-0.5	24.4
Solar wind	-	-
Solar wind irradiated <10 µm Itokawa olivine	0.1-1.2	24
Terrestrial reservoirs		
SMOW	-	-
Bulk Silicate Earth	0.6-3.6	21.2
Earth's Deep Mantle	0.1-1	21.2

*molecular % is defined here by number of water molecules per 100 atoms.

data from Garenne 2014, Greenburg 1998, Szurgot 2005, Anderson and Kovach 1967, Jin and
al., 2017, Robert et al., 2001, Huss et al., 2012, this study, Piani et al 2020, Mccubbin et al 20

molecular % water*	D/H ratio (10^{-6})
2.1-16.4	148 ± 20
2.1-16.4	168 ± 1
2.1-16.4	257 ± 20
0.1-0.8	131 ± 8
0.1-0.7	135 ± 2
-	0.2-20 ± 4
0.1-1.6	0.2-20 ± 4
-	156 ± 0.1
0.9-5.2	149 ± 3
0.2-1.2	122 ± 5

l Bose 2019, Marty 2012, Alexander et
19, Peslier et al 2017